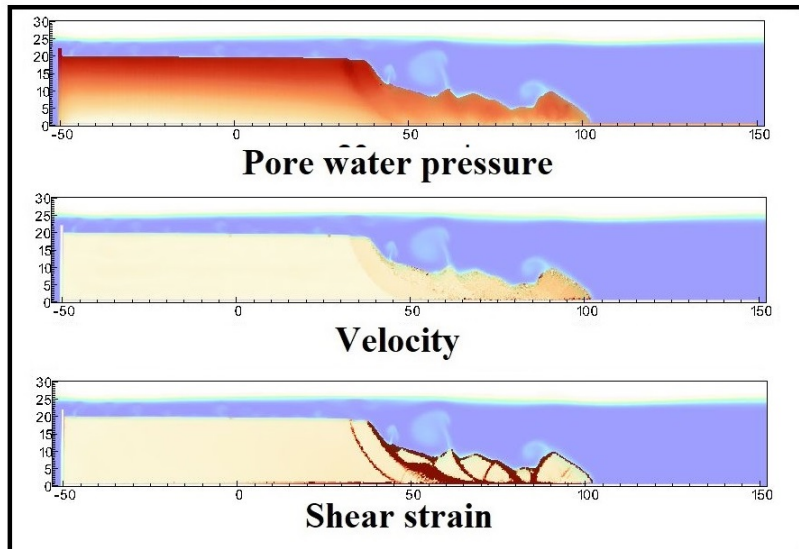


- 1 Graphical Abstract
- 2 MPMICE: A hybrid MPM-CFD model for simulating coupled problems in porous media. Application to earthquake-induced submarine landslides
- 3 Quoc Anh Tran, Gustav Grimstad, Seyed Ali Ghoreishian Amiri



**Application to earthquake-induced submarine landslide**

<sub>6</sub> Highlights

<sub>7</sub> **MPMICE: A hybrid MPM-CFD model for simulating coupled prob-**  
<sub>8</sub> **lems in porous media. Application to earthquake-induced subma-**  
<sub>9</sub> **rine landslides**

<sub>10</sub> Quoc Anh Tran, Gustav Grimstad, Seyed Ali Ghoreishian Amiri

- <sub>11</sub> • MPMICE is introduced for multiphase flow in porous media.
- <sub>12</sub> • Material Point method allows to model large deformation of non-isothermal
- <sub>13</sub> porous media.
- <sub>14</sub> • ICE (compressible multi-material CFD formulation) allows stabilizing
- <sub>15</sub> pore water pressure and turbulent flow.
- <sub>16</sub> • MPMICE is validated and apply to simulate the earthquake-induced
- <sub>17</sub> submarine landslide.

<sup>18</sup> MPMICE: A hybrid MPM-CFD model for simulating  
<sup>19</sup> coupled problems in porous media. Application to  
<sup>20</sup> earthquake-induced submarine landslides

<sup>21</sup> Quoc Anh Tran<sup>a</sup>, Gustav Grimstad<sup>a</sup>, Seyed Ali Ghoreishian Amiri<sup>a</sup>

<sup>a</sup>*Norwegian University of Science and Technology, , Trondheim, 7034, Norway*

---

## <sup>22</sup> Abstract

<sup>23</sup> In this paper, we describe a soil-fluid-structure interaction model that com-  
<sup>24</sup> bines soil mechanics (saturated sediments), fluid mechanics (seawater or air),  
<sup>25</sup> and solid mechanics (structures). The formulation combines the Material  
<sup>26</sup> Point Method, which models large deformation of the porous media and the  
<sup>27</sup> structure, with the Implicit Continuous-fluid Eulerian, which models com-  
<sup>28</sup> plex fluid flows. We validate the model and simulate the whole process of  
<sup>29</sup> earthquake-induced submarine landslides. We show that this model captures  
<sup>30</sup> complex interactions between saturated sediment, seawater, and structure,  
<sup>31</sup> so we can use the model to estimate the impact of potential submarine land-  
<sup>32</sup> slides on offshore structures.

<sup>33</sup> *Keywords:*

<sup>34</sup> Material Point Method, MPMICE, submarine landslide.

---

<b>35</b>	<b>Contents</b>	
<b>36</b>	<b>Nomenclature</b>	<b>4</b>
<b>37</b>	<b>Introduction</b>	<b>6</b>
<b>38</b>	<b>Theory and formulation</b>	<b>8</b>
39	Assumptions . . . . .	8
40	Governing equations . . . . .	9
41	Constitutive soil model . . . . .	11
42	Turbulent model . . . . .	12
43	Frictional force for soil-structure interaction . . . . .	12
44	Momentum and Energy exchange model . . . . .	13
45	Solving momentum and energy exchange with an implicit solver	14
46	Equation of state for fluid phases . . . . .	16
<b>47</b>	<b>Numerical implementation</b>	<b>17</b>
48	Interpolation from Solid Particle to Grid . . . . .	18
49	Compute equation of state for fluid phase . . . . .	20
50	Compute cell face velocity . . . . .	20
51	Compute cell face temperature . . . . .	21
52	Compute fluid pressure (implicit scheme) . . . . .	22
53	Compute viscous shear stress term of the fluid phase . . . . .	22
54	Compute nodal internal temperature of the solid phase . . . . .	22
55	Compute and integrate acceleration of the solid phase . . . . .	23
56	Compute Lagrangian value (mass, momentum and energy) . . . . .	23
57	Compute Lagrangian specific volume of the fluid phase . . . . .	24
58	Compute advection term and advance in time . . . . .	25
59	Interpolate from cell to node of the solid phase . . . . .	26
60	Update the particle variables . . . . .	26
<b>61</b>	<b>Numerical examples</b>	<b>27</b>
62	Fluid Flow through isothermal porous media . . . . .	27
63	Isothermal consolidation . . . . .	28
64	Thermal induced cavity flow . . . . .	29
65	Underwater debris flow . . . . .	30
66	Earthquake-induced submarine landslides . . . . .	34
<b>67</b>	<b>Conclusions</b>	<b>38</b>

68	<b>Acknowledgements</b>	39
69	<b>Appendix: Equation derivation</b>	39
70	Evolution of porosity . . . . .	39
71	Momentum conservation . . . . .	40
72	Energy conservation . . . . .	41
73	Advanced Fluid Pressure . . . . .	42
74	Momentum and Energy exchange with an implicit solver . . . . .	43

<sup>75</sup> **Nomenclature**

**General variables**

<u>Variable</u>	<u>Dimensions</u>	<u>Description</u>
$V$	$[L^3]$	Representative volume
$n$		Porosity
$\sigma$	$[ML^{-1}t^{-2}]$	Total stress tensor
$\Delta t$	$[t]$	Time increment
$\mathbf{b}$	$[ML^1t^{-2}]$	Body force
$c_v$	$[L^2t^{-2}T^{-1}]$	Constant volume specific heat
$f_d$	$[MLt^{-2}]$	Drag forces in momentum exchange term
$f^{int}$	$[MLt^{-2}]$	Internal forces
$f^{ext}$	$[MLt^{-2}]$	External forces
$q_{fs}$	$[MLt^{-2}]$	Heat exchange term
$S$		Weighting function
$\nabla S$		Gradient of weighting function

<sup>76</sup>

**Solid phase**

<u>Variable</u>	<u>Dimensions</u>	<u>Description</u>
$m_s$	$[M]$	Solid mass
$\rho_s$	$[ML^{-3}]$	Solid density
$\phi_s$		Solid volume fraction
$\bar{\rho}_s$	$[ML^{-3}]$	Bulk Solid density
$\mathbf{x}_s$	$[L]$	Solid Position vector
$\mathbf{U}_s$	$[Lt^{-1}]$	Solid Velocity vector
$\mathbf{a}_s$	$[Lt^{-2}]$	Solid Acceleration vector
$\sigma'$	$[ML^{-1}t^{-2}]$	Effective Stress tensor
$\epsilon_s$		Strain tensor
$e_s$	$[L^2t^{-2}]$	Solid Internal energy per unit mass
$T_s$	$[T]$	Solid Temperature
$\mathbf{F}_s$		Solid Deformation gradient
$V_s$	$[L^3]$	Solid Volume

<sup>77</sup>

### Fluid phase

<u>Variable</u>	<u>Dimensions</u>	<u>Description</u>
$m_f$	[M]	Fluid mass
$\rho_f$	[ML <sup>-3</sup> ]	Fluid density
$\phi_f$		Fluid volume fraction
$\bar{\rho}_f$	[ML <sup>-3</sup> ]	Bulk Fluid density
$\mathbf{U}_f$	[Lt <sup>-1</sup> ]	Fluid Velocity vector
$\boldsymbol{\sigma}_f$	[ML <sup>-1</sup> t <sup>-2</sup> ]	Fluid stress tensor
$p_f$	[ML <sup>-1</sup> t <sup>-2</sup> ]	Fluid isotropic pressure
$\boldsymbol{\tau}_f$	[ML <sup>-1</sup> t <sup>-2</sup> ]	Fluid shear stress tensor
$e_f$	[L <sup>2</sup> t <sup>-2</sup> ]	Fluid Internal energy per unit mass
$T_f$	[T]	Fluid Temperature
$v_f$	[L <sup>3</sup> /M]	Fluid Specific volume $\frac{1}{\rho_f}$
$\alpha_f$	[1/T]	Thermal expansion
$\mu$	[ML <sup>-1</sup> t <sup>-1</sup> ]	Fluid viscosity
$V_f$	[L <sup>3</sup> ]	Fluid Volume

### Superscript

<u>Variable</u>	<u>Dimensions</u>	<u>Description</u>
$n$		Current time step
$L$		Lagrangian values
$n + 1$		Next time step

### Subscript

$c$	Cell-centered quantity
$p$	Particle quantity
$i$	Node quantity
$FC$	Cell face quantity
$L, R$	Left and Right cell faces

78     **Introduction**

79     Many geological natural processes and their interactions with man-made  
80     structures are influenced by soil-fluid-structure interactions. The prediction  
81     of these processes requires a tool that can capture complex interactions  
82     between soil, fluid, and structure, such as the process of submarine land-  
83     slides. Indeed, The offshore infrastructure as well as coastal communities  
84     may be vulnerable to submarine landslides. Submarine landslides contain  
85     three stages: triggering, failure, and post-failure. Erosion or earthquakes can  
86     trigger slope failures in the first stage. Following the failure, sediments move  
87     quickly after the post-failure stage. In other words, solid-like sediments will  
88     behave like a fluid after failure. This phase transition makes the simulation  
89     of submarine landslides a challenging task.

90  
91     Due to this phase transition, submarine landslide can be modeled by ei-  
92     ther the Computational Fluid Dynamics (CFD) or the particle-based meth-  
93     ods. For simulating submarine slides, CFD methods solve governing equa-  
94     tions in a full-Eulerian framework [1, 2, 3, 4] with interface capturing tech-  
95     niques. While CFD can handle complex flows (such as turbulent flows), it  
96     cannot account for the triggering mechanism of submarine landslides because  
97     it is not straightforward to consider 'soil constitutive laws' of sediment ma-  
98     terials in the Eulerian framework. In contrast, particle-based methods can  
99     overcome this problem by using the Lagrangian framework. These meth-  
100   ods have been extensively used to simulate landslides, like Material Point  
101   Method (MPM) [5], Smooth Particle Hydro Dynamics [6], Particle Finite  
102   Element Method [7], or Coupled Eulerian Lagrangian Method [8]. For sim-  
103   plicity, these simulations adopt total stress analysis which neglects the pore  
104   pressure development which is key factor triggering slope failures.

105  
106   Recent developments in particle-based methods model the coupling of  
107   fluid flows in porous media by sets of Lagrangian particles. For the MPM  
108   family, it is the double-point MPM ([9, 10, 11]) where fluid particles and  
109   solid particles are overlapped in a single computational grid. Even if fluid  
110   flows are considered, particle-based methods have numerical instability in  
111   modeling the fluid flow, which requires additional numerical treatments such  
112   as the B-bar method [9], null-space filter [12], or least square approximation  
113   [13, 14]. Indeed, CFD is a more optimal option for complex fluid flows  
114   especially dealing with large distortions of continuum fluid media. Therefore,

115 it could be ideal to combine the CFD with particle-based methods. More than  
 116 50 particle-based methods have been developed to solve large deformations  
 117 of solids over the last two decades [15], but the MPM appears to be the  
 118 best candidate for coupling with the CFD. Because MPM incorporates a  
 119 stationary mesh during computation, just like CFD. As such, both MPM  
 120 and CFD can be coupled naturally in a unified computational mesh.



*Figure 1: Interaction between soil-fluid-structure*

121

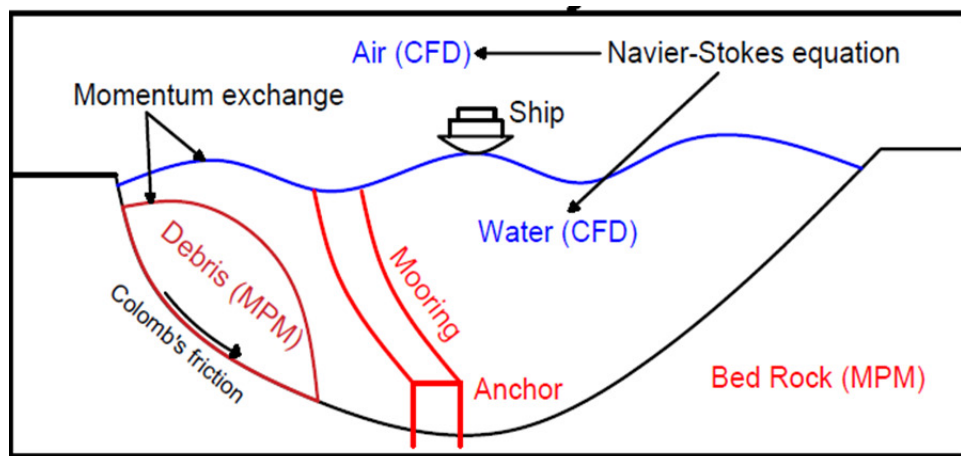


*Figure 2: Coupling of soil-water-structure interaction using MPMICE*

122 A numerical method for simulating soil-fluid-structure interaction (Figure  
123 1) involving large deformations, is presented in this work in order to simu-  
124 late the interaction between sediment (soil), seawater (fluid) and offshore  
125 structures (structure) namely MPMICE (Figure 2). In the MPMICE, the  
126 Material Point Method (MPM) is coupled with the Implicit Continuous Eu-  
127 lerian (ICE). The MPM method is a particle method that allows the porous  
128 soil to undergo arbitrary distortions. The ICE method, on the other hand,  
129 is a conservative finite volume technique with all state variables located at  
130 the cell center (temperature, velocity, mass, pressure). An initial technical  
131 report [16] at Los Alamos National Laboratory provided the theoretical and  
132 algorithmic foundation for the MPMICE, followed by the MPMICE devel-  
133 opment and implementation in the high-performance Uintah computational  
134 framework for simulating fluid-structure interactions [17]. This paper pri-  
135 marily contributes further to the development of the MPMICE for analyzing  
136 the **soil**-fluid-structure interaction, since sediment should be considered as a  
137 porous media (soil) and not as a solid to capture the evolution of the pore  
138 water pressure. Baumgarten et al. [18] made the first attempt at coupling  
139 the Finite Volume Method with the MPM for the simulation of soil-fluid  
140 interaction. In contrast to the mentioned work, we use implicit time integra-  
141 tion for the multi phase flows instead of explicit time integration for the  
142 single-phase flow.

### 143 **Theory and formulation**

144 This section lay out the theoretical framework for the MPMICE model.  
145 We use the common notation of the continuum mechanics with vector and  
146 tensor denoted simply by using bold font and scalar denoted by using normal  
147 font. The notation are shown in Nomenclature.

### 148 *Assumptions*

149 The following assumptions are made for the MPMICE model.

- 150 1. Solid phases (MPM) are described in a Lagrangian formulation while  
151 fluid phases (ICE) are described in an Eulerian formulation in the  
152 framework of continuum mechanics and mixture theory.
- 153 2. Solid grains are incompressible while the fluid phases are compressible.  
154 Solid's thermal expansion is negligible.
- 155 3. There is no mass exchange between solid and fluid phases.
- 156 4. Terzaghi's effective stress is valid.

157 *Governing equations*

158 A representative element volume  $\Omega$  is decomposed by two domains: solid  
159 domains  $\Omega_s$  and fluid domains  $\Omega_f$ . Then, all domains are homogenized  
160 into two overlapping continua. Considering the volume fraction of solid  
161  $\phi_s = \Omega_s/\Omega$  and fluid  $\phi_f = \Omega_f/\Omega$  with the true (or Eulerian) porosity  
162  $n = \sum \phi_f$  of the representative element volume, the average density of solid  
163 and fluid phases are defined as:

164

$$\bar{\rho}_s = \phi_s \rho_s, \quad \bar{\rho}_f = \phi_f \rho_f \quad (1)$$

165 The mass of solid and fluid phases are:

166

$$m_s = \int_{\Omega_s} \rho_s dV = \bar{\rho}_s V, \quad m_f = \int_{\Omega_f} \rho_f dV = \bar{\rho}_f V \quad (2)$$

167 Reviewing the Terzaghi's effective stress concept for the saturated porous  
168 media, the total stress  $\sigma$  is calculated by:

169

$$\sigma = \sigma' - p_f I \quad (3)$$

170 The balance equations are derived based on the mixture theory. The rep-  
171 resentative thermodynamic state of the fluid phases are given by the vector  
172  $[m_f, \mathbf{U}_f, e_f, T_f, v_f]$  which are mass, velocity, internal energy, temperature,  
173 specific volume. The representative state of the solid phases are given by the  
174 vector  $[m_s, \mathbf{U}_s, e_s, T_s, \sigma', p_f]$  which are mass, velocity, internal energy, temper-  
175 ature, effective stress and pore water pressure. The derivation is presented  
176 in detail in the Appendix.

177

---

178 Mass Conservation

179 The mass balance equations for both fluid (e.g., water, air) and solid phases  
180 are:

181

$$\frac{1}{V} \frac{\partial m_f}{\partial t} + \nabla \cdot (m_f \mathbf{U}_f) = 0, \quad \frac{1}{V} \frac{D_s m_s}{Dt} = 0 \quad (4)$$

182 Solving the mass balance equation leads to:

$$\frac{D_s n}{Dt} = \phi_s \nabla \cdot \mathbf{U}_s \quad (5)$$

183

---

184 Momentum Conservation

<sup>185</sup> The momentum balance equations for the fluid phases (e.g., water, air) are:

$$\frac{1}{V} \left[ \frac{\partial(m_f \mathbf{U}_f)}{\partial t} + \nabla \cdot (m_f \mathbf{U}_f \mathbf{U}_f) \right] = -\phi_f \nabla p_f + \nabla \cdot \boldsymbol{\tau}_f + \bar{\rho}_f \mathbf{b} + \sum \mathbf{f}_d \quad (6)$$

<sup>186</sup> The momentum balance equations for the solid phases are:

$$\frac{1}{V} \frac{D_s(m_s \mathbf{U}_s)}{Dt} = \nabla \cdot (\boldsymbol{\sigma}') - \phi_s \nabla p_f + \bar{\rho}_s \mathbf{b} + \sum \mathbf{f}_{fric} - \sum \mathbf{f}_d \quad (7)$$

<sup>187</sup>

---

### <sup>188</sup> Energy Conservation

<sup>189</sup> The internal energy balance equations for the fluid phases (e.g., water, air)  
<sup>190</sup> are:

$$\frac{1}{V} \left[ \frac{\partial(m_f e_f)}{\partial t} + \nabla \cdot (m_f e_f \mathbf{U}_f) \right] = -\bar{\rho}_f p_f \frac{D_f v_f}{Dt} + \boldsymbol{\tau}_f : \nabla \mathbf{U}_f + \nabla \cdot \mathbf{q}_f + \sum q_{sf} \quad (8)$$

<sup>191</sup> The internal energy balance equations for the solid phase are:

$$\frac{m_s}{V} c_v \frac{D_s(T_s)}{Dt} = \boldsymbol{\sigma}' : \frac{D_s(\boldsymbol{\epsilon}_s^p)}{Dt} + \nabla \cdot \mathbf{q}_s - \sum q_{sf} \quad (9)$$

<sup>192</sup> where  $c_v$  is the specific heat at constant volume of the solid materials.

<sup>193</sup>

---

<sup>194</sup> Closing the systems of equations, the following additional models are needed:

<sup>195</sup> (1) A constitutive equation to describe the stress - strain behaviour of solid  
<sup>196</sup> phase (computing effective stress  $\boldsymbol{\sigma}'$ ).

<sup>197</sup> (2) Optional turbulent model to compute the viscous shear stress  $\boldsymbol{\tau}_f$ .

<sup>198</sup> (3) Frictional forces  $\mathbf{f}_{fric}$  for the contact for soil-structure interaction be-  
<sup>199</sup> tween solid/porous materials with the friction coefficient  $\mu_{fric}$ .

<sup>200</sup> (4) Exchange momentum models (computing drag force  $\mathbf{f}_d$ ) for interaction  
<sup>201</sup> between materials.

<sup>202</sup> (5) Energy exchange models (computing temerature exhangre term  $q_{sf}$ ) for  
<sup>203</sup> interaction between materials.

<sup>204</sup> (6) An equation of state to establish relations between thermodynamics vari-  
<sup>205</sup> ables of each fluid materials  $[P_f, \bar{\rho}_f, v_f, T_f, e_f]$ .

<sup>206</sup> Four thermodynamic relations for the equation of states are:

$$\begin{aligned} e_f &= e_f(T_f, v_f) \\ P_f &= P_f(T_f, v_f) \\ \phi_f &= v_f \bar{\rho}_f \\ 0 &= n - \sum_{f=1}^{N_f} v_f \bar{\rho}_f \end{aligned} \quad (10)$$

<sup>207</sup> *Constitutive soil model*

<sup>208</sup> As a result of the explicit MPM formulation, we can derive the constitutive law in the updated Lagrangian framework of "small strain - large deformation". Therefore, the rotation of the particles (representative element volume) is manipulated by rotating the Cauchy stress tensor. First, the deformation gradient is decomposed into the polar rotation tensor  $\mathbf{R}_s^{n+1}$  and stretch tensor  $\mathbf{V}_s^{n+1}$  as:

$$\mathbf{F}_s^{n+1} = \mathbf{V}_s^{n+1} \mathbf{R}_s^{n+1} \quad (11)$$

<sup>214</sup> Then, before calling the constitutive model, the stress and strain rate tensor are rotated to the reference configuration as:

$$\boldsymbol{\sigma}'^{n*} = (\mathbf{R}_s^{n+1})^T \boldsymbol{\sigma}'^{n*} \mathbf{R}_s^{n+1} \quad (12)$$

$$\delta\boldsymbol{\epsilon}^{n*} = (\mathbf{R}_s^{n+1})^T \delta\boldsymbol{\epsilon}_s^{n*} \mathbf{R}_s^{n+1} \quad (13)$$

<sup>217</sup> Using the constitutive model with the input tensors  $\boldsymbol{\sigma}'^{n*}, \delta\boldsymbol{\epsilon}^{n*}$  to compute the Cauchy stress tensor at the advanced time step  $\boldsymbol{\sigma}'^{n+1*}$  then rotating it back to current configuration as:

$$\boldsymbol{\sigma}'^{n+1} = \mathbf{R}_s^{n+1} \boldsymbol{\sigma}'^{n+1*} (\mathbf{R}_s^{n+1})^T \quad (14)$$

<sup>220</sup> In this paper, we adopt the hyper-elastic Neo Hookean model for the structure materials and additionally Mohr-Coulomb failure criteria for the soil (porous media) materials. The Cauchy stress of the hyper-elastic Neo Hookean model can be written as:

$$\boldsymbol{\sigma}' = \frac{\lambda \ln(J)}{J} + \frac{\mu}{J} (\mathbf{F} \mathbf{F}^T - \mathbf{J}) \quad (15)$$

<sup>224</sup> where  $\lambda$  and  $\mu$  are bulk and shear modulus ad  $J$  is the determinant of the deformation gradient  $\mathbf{F}$ . And the yield function  $f$  and flow potentials  $g$  of

<sup>226</sup> the Mohr-Coulomb can be written as:

$$\begin{aligned} f &= \sigma'_1 - \sigma'_3 - 2c' \cos(\phi') - (\sigma'_1 + \sigma'_3) \sin(\phi') \\ g &= \sigma'_1 - \sigma'_3 - 2c' \cos(\psi') - (\sigma'_1 + \sigma'_3) \sin(\psi') \end{aligned} \quad (16)$$

<sup>227</sup> where the  $c'$ ,  $\phi'$  and  $\psi'$  are cohesion and friction angle and dilation angle.  $\sigma'_1$   
<sup>228</sup> and  $\sigma'_3$  are maximum and minimum principal stress.

<sup>229</sup> *Turbulent model*

<sup>230</sup> The turbulent effect is modelled using a statistical approach namely large-  
<sup>231</sup> eddy simulation. In this approach, the micro-scale turbulent influence in the  
<sup>232</sup> dynamics of the macro-scale motion is computed through simple models like  
<sup>233</sup> Smagorinsky model. In the Smagorinsky model, the residual stress tensor is:

$$\tau_{ij} = 2\mu_{eff}(\bar{S}_{ij} - \frac{1}{3}\delta_{ij}\bar{S}_{kk}) + \frac{1}{3}\delta_{ij}\tau_{kk} \quad (17)$$

<sup>234</sup> where the strain rate tensor is given by:

$$\bar{S}_{ij} = \frac{1}{2}(\frac{\delta \bar{U}_i}{\delta x_j} + \frac{\delta \bar{U}_j}{\delta x_i}) \quad (18)$$

<sup>235</sup> and the effective viscosity is sum of molecular viscosity and turbulent viscosity  
<sup>236</sup>  $\mu_{eff} = \mu + \mu_t$  in which the turbulent viscosity  $\mu_t$  is calculated by:

$$\mu_t = (C_s \Delta)^2 \sqrt{2\bar{S}_{ij}\bar{S}_{ij}} \quad (19)$$

<sup>237</sup> where  $C_s$  is the Smagorinsky constant with the value of 0.1 and  $\Delta = \sqrt[3]{dxdydz}$   
<sup>238</sup> is the grid size that defines the subgrid length scale.

<sup>239</sup> *Frictional force for soil-structure interaction*

<sup>240</sup> MPMICE includes a contact law for the interaction between soil and  
<sup>241</sup> structure using the first Coulomb friction contact for MPM presented by  
<sup>242</sup> Bardenhagen et al. ([19]). The magnitude of the friction force at the contact  
<sup>243</sup> depends on the friction coefficient  $\mu_{fric}$  and the normal force  $\mathbf{f}_{norm}$  computed  
<sup>244</sup> from the projection of the contact force in the normal direction.

$$\mathbf{f}_{fric} = \mu_{fric} \mathbf{f}_{norm} \quad (20)$$

245 The contact determines whether the soil is sliding or sticking to the structure  
 246 by comparing the friction force with the sticking force  $\mathbf{f}_{stick}$  computed from  
 247 the projection of the contact force in the tangent direction as:

$$\begin{aligned} \text{if } \mathbf{f}_{fric} \geq \mathbf{f}_{stick} & \text{ no sliding} \\ \text{if } \mathbf{f}_{fric} < \mathbf{f}_{stick} & \text{ sliding occurs} \end{aligned} \quad (21)$$

248 Frictional sliding between solid materials also generates dissipation and the  
 249 work rate generated from the sliding can be calculated as:

$$\Delta W_{friction} = \mathbf{f}_{fric} d \quad (22)$$

250 where  $d$  is the sliding distance which can be computed based on the sliding  
 251 velocity between two materials.

252 *Momentum and Energy exchange model*

253 Currently, the energy exchange coefficient  $H_{sf}$  is assumed to be constant  
 254 for the sake of simplicity. Then the energy exchange can be written as:

$$q_{sf} = H_{sf}(T_f - T_s) \quad (23)$$

255 On the other hand, the drag force can be calculated as:

$$f_d = K(\mathbf{U}_s - \mathbf{U}_f) \quad (24)$$

256 For the momentum exchange between fluid flows and porous media, we as-  
 257 sume that the drag force  $\mathbf{f}_d$  depends on the average grain size of the grains  
 258  $D_p$ , the porosity  $n$ , the fluid viscosity  $\mu_f$ , and is proportional to the relative  
 259 velocities of soil grains and fluid  $(\mathbf{U}_s - \mathbf{U}_f)$ . Based on recent investigation  
 260 of CFD simulations of fluid flow around mono- and bi-disperse packing of  
 261 spheres for  $0.1 < \phi_s < 0.6$  and  $Re < 1000$  [20]. The drag force is given by:

$$\mathbf{f}_d = \frac{18\phi_s(1-\phi_s)\mu_f}{D_p^2} F(\phi_s, Re)(\mathbf{U}_s - \mathbf{U}_f) \quad (25)$$

263 where Reynolds number  $Re$  are computed as:

$$Re = \frac{n\rho_f D_p}{\mu_f} \|(\mathbf{U}_s - \mathbf{U}_f)\| \quad (26)$$

<sup>264</sup> The function  $F(\phi_s, Re)$  can be calculated as:

$$F(\phi_s, Re) = F(\phi_s, 0) + \frac{0.413Re}{24(1 - \phi_s)^2} \left( \frac{(1 - \phi_s)^{-1} + 3\phi_s(1 - \phi_s) + 8.4Re^{-0.343}}{1 + 10^{3\phi_s}Re^{-(1+4\phi_s)/2}} \right) \quad (27)$$

<sup>265</sup> where the low Reynold coefficient  $F(\phi_s, Re \rightarrow 0)$  is:

$$F(\phi_s, 0) = \frac{10\phi_s}{(1 - \phi_s)^2} + (1 - \phi_s)^2(1 + 1.5\sqrt{\phi_s}) \quad (28)$$

<sup>266</sup> When validating the model with analytical solution, it requires to know the  
<sup>267</sup> hydraulic conductivity  $K$ . In such case, we convert the equation (29) to  
<sup>268</sup> Kozeny-Carman formula by assuming  $F(\phi_s, Re) = 10\phi_s/(1 - \phi_s)^2$ , leading to

$$\mathbf{f}_d = \frac{180\phi_s^2\mu_f}{D_p^2(1 - \phi_s)} (\mathbf{U}_s - \mathbf{U}_f) \quad (29)$$

<sup>269</sup> Then, the draging force following the Darcy law is given by:

$$\mathbf{f}_d = \frac{n^2\mu_f}{\kappa} (\mathbf{U}_s - \mathbf{U}_f) \quad (30)$$

<sup>270</sup> where  $\kappa$  being intrinsic permeability of soil which can be written as:

$$\kappa = \frac{K\mu_f}{\rho_f g} \quad (31)$$

<sup>271</sup> As such, the hydraulic conductivity will be expressed as:

$$K = \frac{D_p^2(1 - \phi_s)^3}{180\phi_s^2\mu_f} \rho_f g \quad (32)$$

<sup>272</sup> *Solving momentum and energy exchange with an implicit solver*

<sup>273</sup> The derivation of the implicit integration for the momentum exchange is  
<sup>274</sup> presented in the Appendix's section 'Momentum and energy exchange with  
<sup>275</sup> an implicit solver'. The linear equations for multi phases i,j=1:N has the  
<sup>276</sup> form as:

$$\begin{vmatrix} (1 + \beta_{ij}) & -\beta_{ij} \\ -\beta_{ji} & (1 + \beta_{ji}) \end{vmatrix} \begin{vmatrix} \Delta \mathbf{U}_i \\ \Delta \mathbf{U}_j \end{vmatrix} = \begin{vmatrix} \beta_{ij}(\mathbf{U}_i^* - \mathbf{U}_j^*) \\ \beta_{ji}(\mathbf{U}_i^* - \mathbf{U}_j^*) \end{vmatrix}$$

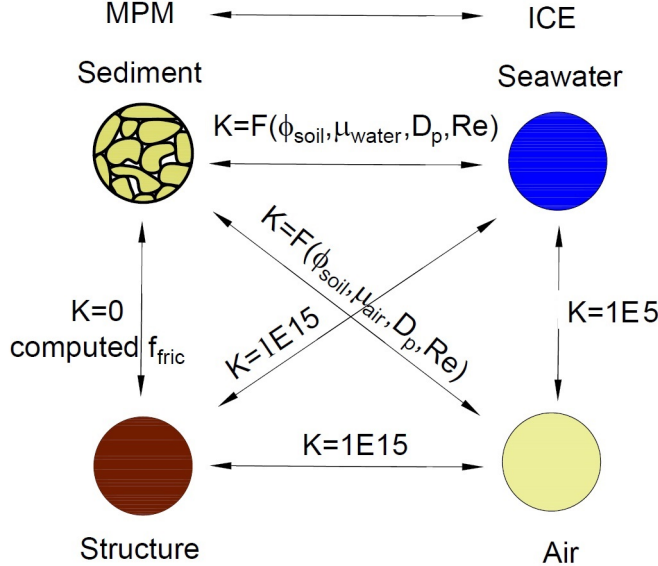


Figure 3: Momentum exchange coefficient between materials

277 where the intermediate velocity for fluid phases  $f=1:N_f$  and for solid/porous  
 278 phases  $s=1:N_s$  can be calculated by:

$$\begin{aligned} U_f^* &= U_f^n + \Delta t \left( -\frac{\nabla P_f^{n+1}}{\rho_f^n} + \frac{\nabla \cdot \tau_f^n}{\bar{\rho}_f^n} + \mathbf{b} \right) \\ U_s^* &= U_s^n + \Delta t \left( \frac{\nabla \cdot \sigma'^n}{\bar{\rho}_s^n} - \frac{\nabla P_f^{n+1}}{\rho_s} + \mathbf{b} \right) \end{aligned} \quad (33)$$

279 Also, the momentum exchange coefficient can be computed at every time  
 280 step as  $\beta_{12} = K/\bar{\rho}_f^n$  and  $\beta_{21} = K/\bar{\rho}_s^n$  with the coefficient depending on the  
 281 different type of interactions (see Figure 3) as for example:

282

- 283 1. The drag force is set to zero in soil-structure interactions, and instead  
 284 the frictional force is computed.  
 285 2. As a result of fluid-structure interaction, the momentum exchange coef-  
 286 ficient should be extremely high ( $1E15$ ) when the solid material points  
 287 are considered to be zero-porosity/zero-permeability.  
 288 3. In the case of soil-fluid interaction, the drag force is calculated using  
 289 the equation (29). Considering that air has a much lower viscosity than

water, its drag force is much lower than the drag force of water in a pore.

- 292     4. A momentum exchange coefficient of 1E5 is applied between multiphase  
 293       flows. This value is far higher than reality [21], but it is necessary to  
 294       have enough numerical stability to conduct simulations in the numerical  
 295       example.

296     Similar approach applied for the energy exchange term leading to:

$$\begin{vmatrix} (1 + \eta_{ij}) & -\eta_{ij} \\ -\eta_{ji} & (1 + \eta_{ji}) \end{vmatrix} \begin{vmatrix} \Delta T_i \\ \Delta T_j \end{vmatrix} = \begin{vmatrix} \eta_{ij}(T_i^n - T_j^n) \\ \eta_{ji}(T_j^n - T_i^n) \end{vmatrix}$$

297     with  $\eta$  being the energy exchange coefficient.

298     *Equation of state for fluid phases*

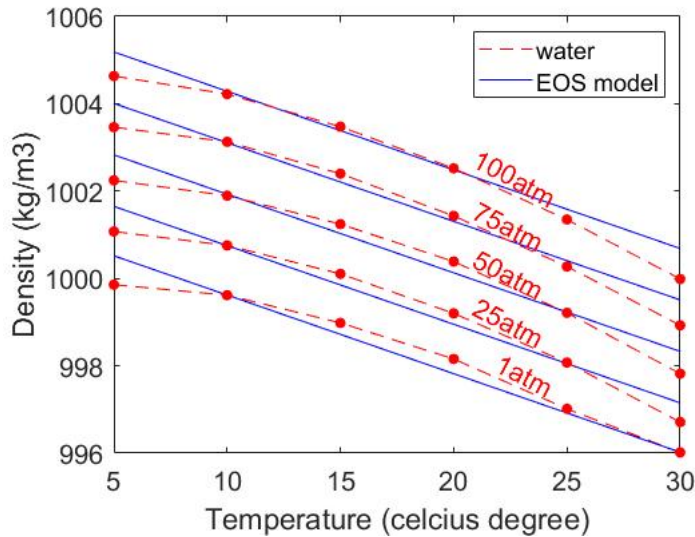


Figure 4: Equation of state of water

299     The equation of state establishes relations between thermodynamics vari-  
 300       ables  $[P_f, \rho_f, T_f]$ . The choice of the equation of state depends on the types  
 301       of the fluid materials. For example, for the air, it is possible to assume the  
 302       equation of state for the perfect gas which obeys:

$$P_f = \rho_f R T_f \quad (34)$$

303 where  $R$  is the gas constant. For the water, a simple linear equation of state  
 304 is in the following form:

$$P_f = P_{ref} + K_f(\rho_f - \rho_{ref} - \alpha_f(T_f - T_{ref})) \quad (35)$$

305 where reference pressure  $P_{ref} = 1 \text{ atm} = 101325 \text{ Pa}$ , reference temperature  
 306  $T_{ref} = 10^\circ\text{C}$ , reference density  $\rho_{ref} = 999.8 \text{ kg/m}^3$ , the bulk modulus of water  
 307  $K_f = 2 \text{ GPa}$ , and the water thermal expansion  $\alpha_f = 0.18 \text{ }^\circ\text{C}^{-1}$ . Equation  
 308 (35) matches well with the state of the water (see Figure 4).

309 **Numerical implementation**

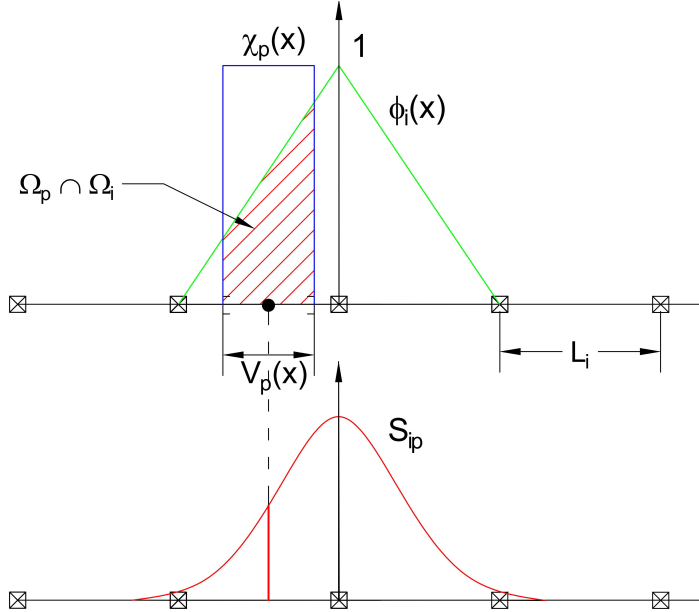


Figure 5: GIMP weighting function (red as a convolution of the linear basis shape function (green) and the characteristic function (blue))

310 The fluid phases are discretized in the grid with the state variables stored  
 311 at the centroid of the cells  $[\rho_{f,c}, \mathbf{U}_{f,c}, T_{f,c}, v_{f,c}]$  while the solid phase is dis-  
 312 cretized in the particles with the state variables  $[m_{sp}, \mathbf{U}_{sp}, T_{sp}, \boldsymbol{\sigma}'_{sp}]$ . In the  
 313 Material Point Method, we use the generalized interpolation technique [22]  
 314 using the weight function as a convolution of a grid shape function  $N_i(\mathbf{x})$  in

<sup>315</sup> a nodal domain  $\Omega_i$  and a characteristic function  $\chi_p(\mathbf{x})$  in a particle domain  
<sup>316</sup>  $\Omega_p$  with the volume  $V_p(\mathbf{x})$  as follows:

$$S_{ip} = \frac{1}{V_p} \int_{\Omega_i \cap \Omega_p} N_i(\mathbf{x}) \chi_p(\mathbf{x}) d\mathbf{x} \quad (36)$$

<sup>317</sup> where the volume  $V_p(\mathbf{x})$  of the material point p can be calculated as:

$$V_p = \int_{\Omega_p} \chi_p(\mathbf{x}) d\mathbf{x} \quad (37)$$

<sup>318</sup> The characteristic function is the Heaviside function as  $\chi_p = 1$  if  $\mathbf{x} \in \Omega_p$ ,  
<sup>319</sup> otherwise 0 (see Figure 5). For the interpolation of the centroid of the cell,  
<sup>320</sup> the linear basis function is used as:

$$S_{ci} = N_i(\mathbf{x}_c) \quad (38)$$

<sup>321</sup> The time discretization are solved using the following steps.

### <sup>322</sup> *Interpolation from Solid Particle to Grid*

<sup>323</sup> The nodal values of the solid state (mass, velocity, temperature, volume)  
<sup>324</sup> are:

$$\begin{aligned} m_{si}^n &= \sum S_{ip} m_{sp} \\ \mathbf{U}_{si}^n &= \frac{\sum S_{ip} (m\mathbf{U})_{sp}^n}{m_{si}^n} \\ T_{si}^n &= \frac{\sum S_{ip} (mT)_{sp}^n}{m_{si}^n} \\ V_{si}^n &= \frac{\sum S_{ip} (mV)_{sp}^n}{m_{si}^n} \\ \boldsymbol{\sigma}_{si}^n &= \frac{\sum S_{ip} (\boldsymbol{\sigma}V)_{sp}^n}{V_{si}^n} \end{aligned} \quad (39)$$

<sup>325</sup> The nodal internal forces is calculated by:

$$\mathbf{f}_{si}^{int,n} = - \sum \nabla S_{ip} (\boldsymbol{\sigma}'_{sp})^n V_{sp}^n \quad (40)$$

<sup>326</sup> The nodal external forces  $f_{si}^{ext,n}$  and the nodal frictional forces  $f_{si}^{fric}$  from  
<sup>327</sup> contact between materials are computed here.

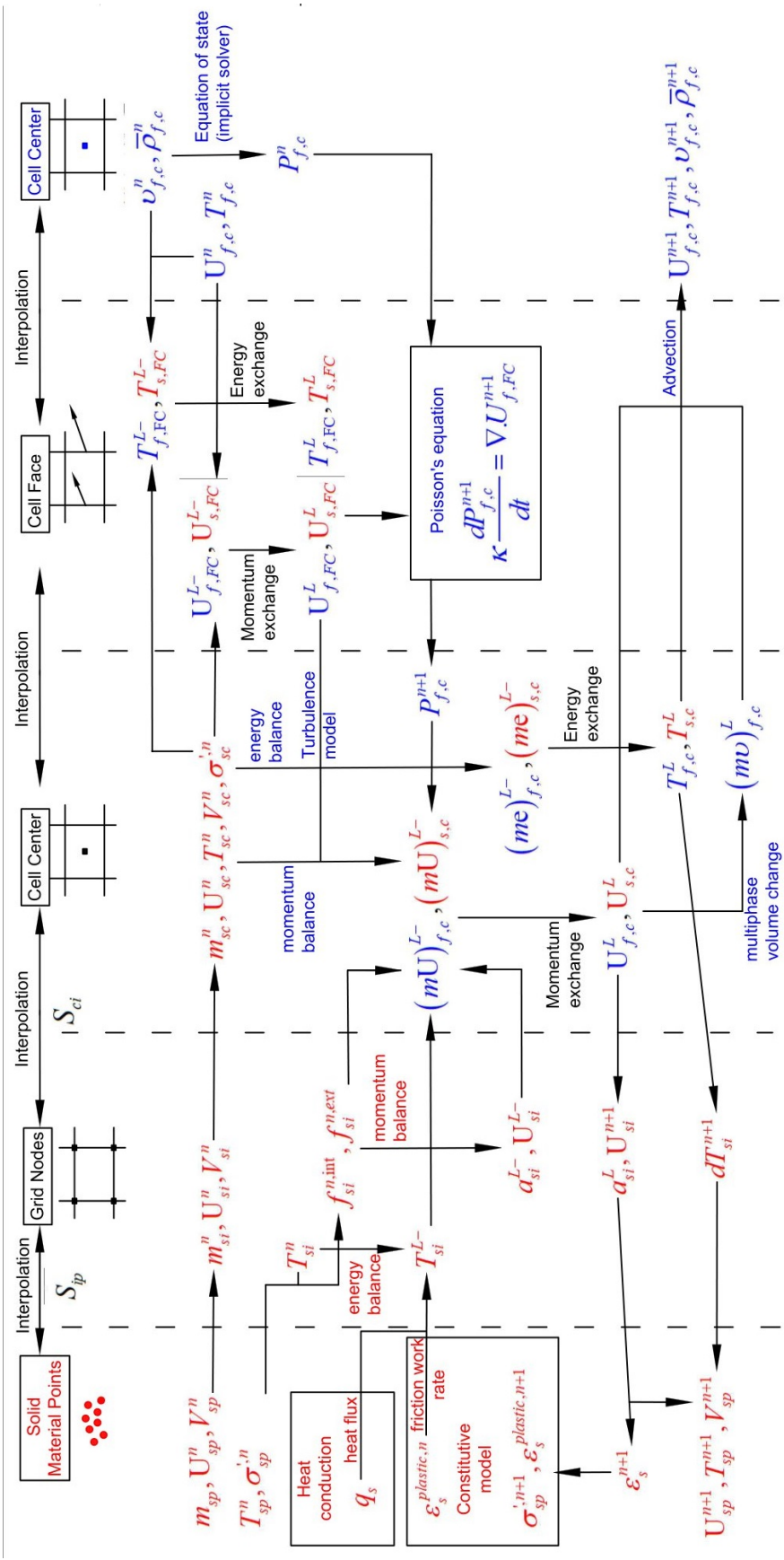


*Figure 6: Numerical implementation of MPMICE*

<sup>328</sup> Then we compute the solid cell variables as:

$$\begin{aligned}
 m_{sc}^n &= \sum S_{ci} m_{si} \\
 \rho_{sc}^n &= \frac{m_{sc}^n}{V} \\
 \mathbf{U}_{sc}^n &= \sum S_{ci} \mathbf{U}_{si}^n \\
 T_{sc}^n &= \sum S_{ci} T_{si}^n \\
 V_{sc}^n &= \sum S_{ci} V_{si}^n \\
 \boldsymbol{\sigma}_{sc}^n &= \sum S_{ci} \boldsymbol{\sigma}_{si}^n
 \end{aligned} \tag{41}$$

<sup>329</sup> *Compute equation of state for fluid phase*

<sup>330</sup> The total fluid material volume of a cell is:

$$V_{total} = \sum_{f=1}^{N_f} M_f v_f \tag{42}$$

<sup>331</sup> We need to find  $P_{f,c}^n$  which allows each fluid materials obey their equation of  
<sup>332</sup> states  $[P_f, \rho_f, v_f, T_f, e_f]$  but also allow mass of all fluid materials to fill the  
<sup>333</sup> entire the pore volume without ongoing compression or expansion following  
<sup>334</sup> the condition as follows:

$$0 = n - \sum_{f=1}^{N_f} v_f \bar{\rho}_f \tag{43}$$

<sup>335</sup> Then, we can use the Newton-Raphson interation to find the value of  $P_{f,c}^n$   
<sup>336</sup> which satisfies the equation (42, 43) and each equation of states of each fluid  
<sup>337</sup> materials.

<sup>338</sup> *Compute cell face velocity*

<sup>339</sup> Following the derivation in the Appendix: Advanced Fluid Pressure, we  
<sup>340</sup> first compute the fluid cell face velocity as:

$$\mathbf{U}_{f,FC}^{L-} = \frac{(\bar{\rho} \mathbf{U})_{f,FC}^n}{\bar{\rho}_{f,FC}^n} + \Delta t \left( -\frac{\nabla^{FC} P_{f,c}^n}{\bar{\rho}_{f,FC}^n} + \frac{\nabla^{FC} \cdot \boldsymbol{\tau}^n}{\bar{\rho}_{s,FC}} + \mathbf{b} \right) \tag{44}$$

<sup>341</sup> The equation (44) is discretized in three dimension (noted that  $\nabla^{FC} \cdot \boldsymbol{\tau} = 0$ ),  
<sup>342</sup> for example the discretized equation in the x direction is:

$$U_{fx}^{L-} = \frac{(\bar{\rho} U)_{fx,R}^n + (\bar{\rho} U)_{fx,L}^n}{\bar{\rho}_{fx,L}^n + \bar{\rho}_{fx,R}^n} + \Delta t \left( -\frac{2(v_{fx,L}^n v_{fx,R}^n)}{v_{fx,L}^n + v_{fx,R}^n} \frac{P_{f,cx,R}^n - P_{f,cx,L}^n}{\Delta x} + b_x \right) \tag{45}$$

<sup>343</sup> The cell face solid velocity can be calculated as:

$$\mathbf{U}_{s,FC}^{L-} = \frac{(\bar{\rho}\mathbf{U})_{s,FC}^n}{\bar{\rho}_{s,FC}^n} + \Delta t \left( \frac{\nabla^{FC} \cdot \boldsymbol{\sigma}_c'^n}{\bar{\rho}_{s,FC}} - \frac{\nabla^{FC} P_{f,c}^n}{\rho_s} + \mathbf{b} \right) \quad (46)$$

<sup>344</sup> The equation (46) is discretized in three dimension (noted that  $\nabla^{FC} \cdot \boldsymbol{\sigma}_{ij} = 0$   
<sup>345</sup> with  $i \neq j$ ), for example the discretized equation in the x direction is:

$$U_{sx}^{L-} = \frac{(\bar{\rho}U)_{sx,R}^n + (\bar{\rho}U)_{sx,L}^n}{\bar{\rho}_{sx,L}^n + \bar{\rho}_{sx,R}^n} + \Delta t \left( \frac{2(\sigma_{xx,R} - \sigma_{xx,L})}{(\bar{\rho}_{sx,L}^n + \bar{\rho}_{sx,R}^n)\Delta x} - \frac{P_{f,cx,R}^n - P_{f,cx,L}^n}{\rho_s \Delta x} + b_x \right) \quad (47)$$

<sup>346</sup> Then, we compute the modified cell face velocity  $\mathbf{U}_{FC}^L$  considering the mo-  
<sup>347</sup> mentum exchange (see the Appendix: Momentum exchange with an implicit  
<sup>348</sup> solve) as follows:

$$\begin{aligned} \mathbf{U}_{f,FC}^L &= \mathbf{U}_{f,FC}^{L-} + \Delta \mathbf{U}_{f,FC} \\ \mathbf{U}_{s,FC}^L &= \mathbf{U}_{s,FC}^{L-} + \Delta \mathbf{U}_{s,FC} \end{aligned} \quad (48)$$

<sup>349</sup> The linear equation below is solved to obtain the increment of velocity with  
<sup>350</sup>  $i,j = 1 : N$  as:

$$\begin{vmatrix} (1 + \beta_{ij}) & -\beta_{ij} \\ -\beta_{ji} & (1 + \beta_{ji}) \end{vmatrix} \begin{vmatrix} \Delta \mathbf{U}_{i,FC} \\ \Delta \mathbf{U}_{j,FC} \end{vmatrix} = \begin{vmatrix} \beta_{ij}(\mathbf{U}_{i,FC}^{L-} - \mathbf{U}_{j,FC}^{L-}) \\ \beta_{ji}(\mathbf{U}_{j,FC}^{L-} - \mathbf{U}_{i,FC}^{L-}) \end{vmatrix}$$

### <sup>351</sup> Compute cell face temperature

<sup>352</sup> Similar to the velocity, the faced temperature is computed, for example  
<sup>353</sup> in x direction, as:

$$\begin{aligned} T_{fx}^{L-} &= \frac{(\bar{\rho}T)_{fx,R}^n + (\bar{\rho}T)_{fx,L}^n}{\bar{\rho}_{fx,L}^n + \bar{\rho}_{fx,R}^n} \\ T_{sx}^{L-} &= \frac{(\bar{\rho}T)_{sx,R}^n + (\bar{\rho}T)_{sx,L}^n}{\bar{\rho}_{sx,L}^n + \bar{\rho}_{sx,R}^n} \end{aligned} \quad (49)$$

<sup>354</sup> Then, we compute the modified cell face temperature  $T_{FC}^L$  considering the  
<sup>355</sup> energy exchange (see the Appendix: Momentum and energy exchange with  
<sup>356</sup> an implicit solver) as follows:

$$\begin{aligned} T_{f,FC}^L &= T_{f,FC}^{L-} + \Delta T_{f,FC} \\ T_{s,FC}^L &= T_{s,FC}^{L-} + \Delta T_{s,FC} \end{aligned} \quad (50)$$

<sup>357</sup> The linear equation below is solved to determine the increment of velocity  
<sup>358</sup> with  $i,j = 1 : N$  as:

$$\begin{vmatrix} (1 + \eta_{ij}) & -\eta_{ij} \\ -\eta_{ji} & (1 + \eta_{ji}) \end{vmatrix} \begin{vmatrix} \Delta T_{i,FC} \\ \Delta T_{j,FC} \end{vmatrix} = \begin{vmatrix} \eta_{ij}(T_{i,FC}^{L-} - T_{j,FC}^{L-}) \\ \eta_{ji}(T_{j,FC}^{L-} - T_{i,FC}^{L-}) \end{vmatrix}$$

359    ***Compute fluid pressure (implicit scheme)***

360    For single phase flow, the increment of the fluid pressure can be computed  
361    as:

$$\kappa_f \frac{\Delta P}{dt} = \nabla^c \cdot \mathbf{U}_{f,FC}^{n+1} \quad (51)$$

362    For multi-phase flows, the increment of the fluid pressure of the mixture can  
363    be computed as:

$$\kappa \frac{\Delta P}{dt} = \sum_{f=1}^{N_f} \nabla^c \cdot (\phi_{f,FC} \mathbf{U}_{f,FC})^{n+1} \quad (52)$$

364    where  $\kappa = \sum_{f=1}^{N_f} (\phi_{f,FC} \kappa_f) / \sum_{f=1}^{N_f} (\phi_{f,FC})$ . Then, the fluid pressure at cell  
365    center is:

$$P_c^{n+1} = P_c^n + \Delta P_c^n \quad (53)$$

366    Finally, the cell face advanced fluid pressure is:

$$P_{FC}^{n+1} = \left( \frac{P_{c,L}^{n+1}}{\bar{\rho}_{f,L}^n} + \frac{P_{c,R}^{n+1}}{\bar{\rho}_{f,R}^n} \right) / \left( \frac{1}{\bar{\rho}_{f,L}^n} + \frac{1}{\bar{\rho}_{f,R}^n} \right) = \left( \frac{P_{c,L}^{n+1} \bar{\rho}_{f,R}^n + P_{c,R}^{n+1} \bar{\rho}_{f,L}^n}{\bar{\rho}_{f,L}^n \bar{\rho}_{f,R}^n} \right) \quad (54)$$

367    ***Compute viscous shear stress term of the fluid phase***

368    This part compute the viscous shear stress  $\Delta(m\mathbf{U})_{f,c,\tau}$  for a single vis-  
369    cous compressible Newtonian fluid and optionally shear stress induced by the  
370    turbulent model.

371    ***Compute nodal internal temperature of the solid phase***

372    The nodal internal temperature rate is computed based on the heat con-  
373    duction model as below:

$$dT_{si}^{L-} = \frac{(\Delta W_{si}^n + \Delta W_{fric,i}^n + \nabla^i \cdot \mathbf{q}_{si}^n)}{m_{si}^n c_v} \quad (55)$$

374    where  $\Delta W_{si}^n = \boldsymbol{\sigma}' : \frac{D_s(\boldsymbol{\epsilon}_s^p)}{Dt}$  is the mechanical work rate computed from the  
375    constitutive model with  $\boldsymbol{\epsilon}_s^p$  is the plastic strain,  $\Delta W_{fric,i}^n$  is the work rate  
376    computed from the contact law due to the frictional sliding between solid  
377    materials. The heat flux is  $\mathbf{q}_s = \bar{\rho}_s \beta_s \nabla T_s$  with  $\beta_s$  being the thermal conduc-  
378    tivity of the solid materials.

$$T_{si}^{L-} = T_{si}^n + dT_{si}^{L-} \quad (56)$$

379 *Compute and integrate acceleration of the solid phase*

380 After interpolating from material points to the nodes, the nodal acceleration  
381 and velocity are calculated by:

$$\mathbf{a}_{si}^{L-} = \frac{\mathbf{f}_{si}^{int,n} + \mathbf{f}_{si}^{ext,n}}{m_{si}^n} + \mathbf{g} \quad (57)$$

382

$$\mathbf{U}_{si}^{L-} = \mathbf{U}_{si}^n + \mathbf{a}_{si}^{L-} \Delta t \quad (58)$$

383 *Compute Lagrangian value (mass, momentum and energy)*

384 For the fluid phase, the linear momentum rate, the energy rate are:

$$\Delta(m\mathbf{U})_{f,c} = V n_c^n \nabla^c P_c^{n+1} + \Delta(m\mathbf{U})_{f,c,\tau} + V \bar{\rho}_{f,c}^n g \quad (59)$$

385

$$\Delta(me)_{f,c} = V n_c^n P_c^{n+1} \nabla^c \cdot \mathbf{U}_{f,FC}^* + \nabla^c \cdot \mathbf{q}_{f,c}^n \quad (60)$$

386 The Lagrangian value of the mass, linear momentum and energy of fluid  
387 phases without momentum exchange are:

388

$$m_{f,c}^L = V \bar{\rho}_{f,c}^n \quad (61)$$

389

$$(m\mathbf{U})_{f,c}^{L-} = V \bar{\rho}_{f,c}^n \mathbf{U}_{f,c}^n + \Delta(m\mathbf{U})_{f,c} \quad (62)$$

390

$$(me)_{f,c}^{L-} = V \bar{\rho}_{f,c}^n T_{f,c}^n c_v + \Delta(me)_{f,c} \quad (63)$$

391 For the solid phase, the Lagrangian value of the linear momentum and energy  
392 of solid phase are:

393

$$m_{sc}^L = m_{sc}^n \quad (64)$$

394

$$(m\mathbf{U})_{sc}^{L-} = \sum S_{ci} m_{si}^n \mathbf{U}_{si}^{L-} + V(1 - n_c^n) \nabla^c P_{f,c}^{n+1} \quad (65)$$

395

$$(me)_{sc}^{L-} = \sum S_{ci} m_{si}^n T_{si}^L c_v \quad (66)$$

396 To consider the momentum exchange, the Lagrangian velocity is modified as:

$$\begin{aligned} \mathbf{U}_{f,c}^L &= \mathbf{U}_{f,c}^{L-} + \Delta \mathbf{U}_{f,c} \\ \mathbf{U}_{sc}^L &= \mathbf{U}_{sc}^{L-} + \Delta \mathbf{U}_{sc} \end{aligned} \quad (67)$$

397 where the cell-centered intermediate velocity can be calculated by:

$$\begin{aligned} \mathbf{U}_{f,c}^{L-} &= \frac{(m\mathbf{U})_{f,c}^{L-}}{m_{f,c}^L} \\ \mathbf{U}_{sc}^{L-} &= \frac{(m\mathbf{U})_{sc}^{L-}}{m_{sc}^L} \end{aligned} \quad (68)$$

396 And the increment of the velocity  $\mathbf{U}_{f,c}$ ,  $\Delta\mathbf{U}_{sc}$  can be computed by solving  
 397 the linear equation with  $i,j = 1 : N$  as:

$$\begin{vmatrix} (1 + \beta_{ij}) & -\beta_{ij} \\ -\beta_{ji} & (1 + \beta_{ji}) \end{vmatrix} \begin{vmatrix} \Delta\mathbf{U}_{i,c} \\ \Delta\mathbf{U}_{j,c} \end{vmatrix} = \begin{vmatrix} \beta_{ij}(\mathbf{U}_{i,c}^{L-} - \mathbf{U}_{j,c}^{L-}) \\ \beta_{ji}(\mathbf{U}_{j,c}^{L-} - \mathbf{U}_{i,c}^{L-}) \end{vmatrix}$$

398 To consider the energy exchange, the Lagrangian temperature is modified as:

$$\begin{aligned} T_{f,c}^L &= T_{f,c}^{L-} + \Delta T_{f,c} \\ T_{sc}^L &= T_{sc}^{L-} + \Delta T_{sc} \end{aligned} \quad (69)$$

399 where the cell-centered intermediate temperature can be calculated by:

$$\begin{aligned} T_{f,c}^{L-} &= \frac{(mT)_{f,c}^{L-}}{m_{f,c}^L c_v} \\ T_{sc}^{L-} &= \frac{(mT)_{sc}^{L-}}{m_{sc}^L c_v} \end{aligned} \quad (70)$$

400 And the increment of the velocity can be computed by solving the linear  
 401 equation with  $i,j = 1 : N$  as:

$$\begin{vmatrix} (1 + \eta_{ij}) & -\eta_{ij} \\ -\eta_{ji} & (1 + \eta_{ji}) \end{vmatrix} \begin{vmatrix} \Delta T_{i,c} \\ \Delta T_{j,c} \end{vmatrix} = \begin{vmatrix} \eta_{ij}(T_{i,c}^{L-} - T_{j,c}^{L-}) \\ \eta_{ji}(T_{j,c}^{L-} - T_{i,c}^{L-}) \end{vmatrix}$$

402 Finally, we obtain the cell-centered solid acceleration and temperature rate  
 403 as:

$$d\mathbf{U}_{sc}^L = \frac{(m\mathbf{U})_{sc}^L - (m\mathbf{U})_{sc}^n}{m_{sc}^L \Delta t} \quad (71)$$

$$dT_{sc}^L = \frac{(me)_{sc}^L - (me)_{sc}^n}{m_{sc}^L c_v \Delta t} \quad (72)$$

#### 405 Compute Lagrangian specific volume of the fluid phase

406 To compute the Lagrangian value of the specific volume of the fluid phase,  
 407 we need to compute the Lagrangian temperature rate as below:

$$T_{f,c}^{n+1} = \frac{(me)_{f,c}^L}{m_{f,c}^L c_v} \quad (73)$$

$$\frac{D_f T_{f,c}}{Dt} = \frac{T_{f,c}^{n+1} - T_{f,c}^n}{\Delta t} \quad (74)$$

<sup>409</sup> As such, the Lagrangian specific volume rate is:

$$\Delta(mv)_{f,c} = V f_{f,c}^\phi \nabla \cdot \mathbf{U} + (\phi_{f,c} \alpha_{f,c} \frac{D_f T_{f,c}}{Dt} - f_{f,c}^\phi \sum_{n=1}^N \phi_{nc} \alpha_{nc} \frac{D_n T_{n,c}}{Dt}) \quad (75)$$

<sup>410</sup> where  $f_f^\phi = (\phi_f \kappa_f) / (\sum_{n=1}^N \phi_n \kappa_n)$  and  $\mathbf{U} = \nabla \cdot (\sum_{s=1}^{N_s} \phi_{sc} \mathbf{U}_{sc} + \sum_{f=1}^{N_f} \phi_{fc} \mathbf{U}_{f,c})$ .

<sup>411</sup> Finally, the Lagrangian specific volume is:

$$(mv)_{f,c}^L = V \bar{\rho}_{f,c}^n v_{f,c}^n + \Delta(mv)_{f,c} \quad (76)$$

<sup>412</sup> *Compute advection term and advance in time*

<sup>413</sup> The time advanced mass, linear momentum, energy and specific volume  
<sup>414</sup> are:

$$m_{f,c}^{n+1} = m_{f,c}^L - \Delta t \nabla \cdot (\bar{\rho}_{f,c}^L, \mathbf{U}_{f,FC}^L) \quad (77)$$

$$(m\mathbf{U})_{f,c}^{n+1} = (m\mathbf{U})_{f,c}^L - \Delta t \nabla \cdot ((\bar{\rho}\mathbf{U})_{f,c}^L, \mathbf{U}_{f,FC}^L) \quad (78)$$

$$(me)_{f,c}^{n+1} = (me)_{f,c}^L - \Delta t \nabla \cdot ((\bar{\rho}c_v T)_{f,c}^L, \mathbf{U}_{f,FC}^L) \quad (79)$$

$$(mv)_{f,c}^{n+1} = (mv)_{f,c}^L - \Delta t \nabla \cdot ((\bar{\rho}v)_{f,c}^L, \mathbf{U}_{f,FC}^L) \quad (80)$$

<sup>418</sup> Finally, the state variables of the fluid phases of the next time step are:

$$\bar{\rho}_{f,c}^{n+1} = \frac{m_{f,c}^{n+1}}{V} \quad (81)$$

$$\mathbf{U}_{f,c}^{n+1} = \frac{(m\mathbf{U})_{f,c}^{n+1}}{m_{f,c}^{n+1}} \quad (82)$$

$$T_{f,c}^{n+1} = \frac{(me)_{f,c}^{n+1}}{m_{f,c}^{n+1}} \quad (83)$$

$$v_{f,c}^{n+1} = \frac{(mv)_{f,c}^{n+1}}{m_{f,c}^{n+1}} \quad (84)$$

422    *Interpolate from cell to node of the solid phase*

423    First we interpolate the acceleration, velocity and temperature rate to  
424    the node as below:

$$425 \quad \mathbf{a}_{si}^n = \sum S_{ci} d\mathbf{U}_{sc}^L \quad (85)$$

$$425 \quad \mathbf{U}_{si}^{n+1} = \sum S_{ci} d\mathbf{U}_{sc}^L \Delta t \quad (86)$$

$$426 \quad dT_{si}^n = \sum S_{ci} dT_{sc}^L \quad (87)$$

427    Then the boundary condition and contact forces  $f_{si}^{fric}$  are applied to the nodal  
428    velocity and the acceleration is modified by:

$$429 \quad \mathbf{a}_{si}^n = \frac{\mathbf{v}_{si}^{n+1} - \mathbf{v}_{si}^n}{\Delta t} \quad (88)$$

429    *Update the particle variables*

430    The state variables of the solid phase  $[\mathbf{U}_{sp}^{n+1}, \mathbf{x}_{sp}^{n+1}, \nabla \mathbf{U}_{sp}^{n+1}, T_{sp}^{n+1}, \nabla T_{sp}^{n+1}, \mathbf{F}_{sp}^{n+1}, V_{sp}^{n+1}]$   
431    (velocity, position, velocity gradient, temperature, temperature gradient, de-  
432    formation gradient, volume) are updated as:

$$433 \quad \mathbf{U}_{sp}^{n+1} = \mathbf{U}_{sp}^n + \sum S_{sp} \mathbf{a}_{si}^n \Delta t \quad (89)$$

$$434 \quad \mathbf{x}_{sp}^{n+1} = \mathbf{x}_{sp}^n + \sum S_{sp} \mathbf{U}_{si}^{n+1} \Delta t \quad (90)$$

$$435 \quad \nabla \mathbf{U}_{sp}^{n+1} = \sum \nabla S_{sp} \mathbf{U}_{si}^{n+1} \quad (91)$$

$$436 \quad T_{sp}^{n+1} = T_{sp}^n + \sum S_{sp} dT_{si}^n \Delta t \quad (92)$$

$$436 \quad \nabla T_{sp}^{n+1} = \sum \nabla S_{sp} T_{sp}^n \Delta t \quad (93)$$

$$437 \quad \mathbf{F}_{sp}^{n+1} = (\mathbf{I} + \nabla \mathbf{U}_{sp}^{n+1} \Delta t) \mathbf{F}_{sp}^n \quad (94)$$

$$438 \quad V_{sp}^{n+1} = \det(\mathbf{F}_{sp}^{n+1}) V_{sp}^o \quad (95)$$

439    Finally, the effective stress  $(\boldsymbol{\sigma}')^{n+1}$  is updated from the constitutive model  
440    and the pore water pressure is interpolated from the cell as:

$$439 \quad p_f^{n+1} = \sum S_{si} P_c^{n+1} \quad (96)$$

441 **Numerical examples**

442 All input files and the analytical calculations in this section are provided  
 443 in the Github repository ([https://github.com/QuocAnh90/Uintah\\_NTNU](https://github.com/QuocAnh90/Uintah_NTNU))  
 444 for the reproduction of the numerical results.

445 To prevent repetition, we present the parameters of water and air, which  
 446 remain consistent across all simulations. The water has a bulk modulus of 2  
 447 GPa, a density of 998 kg/m<sup>3</sup> at a reference temperature of 5 degrees Celsius  
 448 and a reference pressure of 10325 Pa (1atm), a dynamic viscosity  $\mu_f$  of 1  
 449 mPa s). The air has a ideal gas with a density of 1.17 kg/m<sup>3</sup> at a reference  
 450 temperature of 5 degrees Celsius and a reference pressure of 10325 Pa (1atm),  
 451 a dynamic viscosity  $\mu_f$  of  $18.45E^{-3}$  mPa s).

452 *Fluid Flow through isothermal porous media*

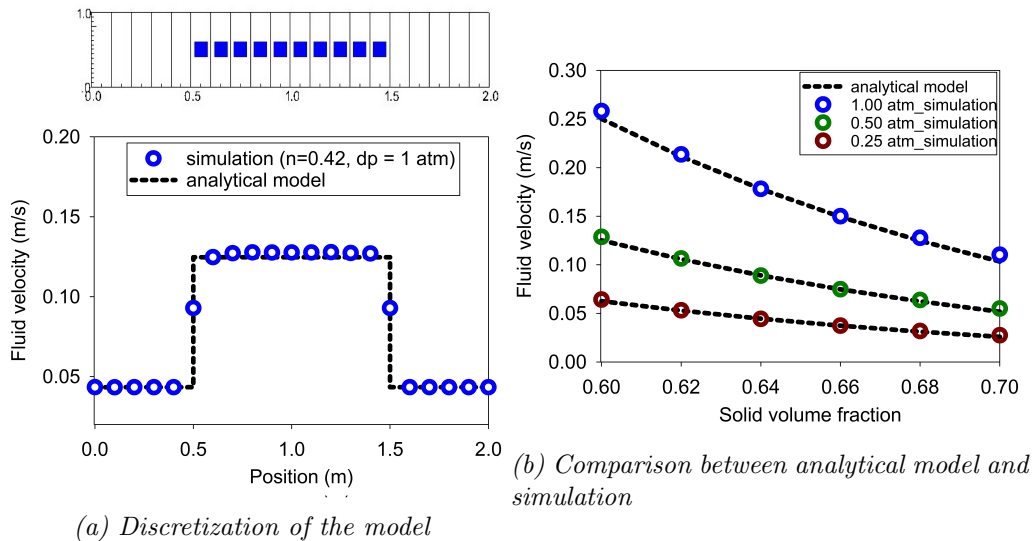


Figure 7: Numerical results of the fluid flow through isothermal porous media

453 Fluid flow through porous media is important in many engineering disci-  
 454 plines, like predicting water flow in soil. Fluid flow velocity in one dimension  
 455 can be calculated from the porous media's hydraulic conductivity  $K$  as:

456

$$U_f = K \frac{\Delta p_f}{L} \quad (97)$$

457 If the Carman-Kozeny formula is adopted  $F = 10\phi_s/(1 - \phi_s)^2$ , the hydraulic  
 458 conductivity will be expressed as  $K = D_p^2(1 - \phi_s)^3\rho_f g/180\phi_s^2\mu_f$ . Then, the  
 459 analytical formula of average velocity in one dimension through the porous  
 460 media is:

461

$$U_f = \frac{1}{n} \frac{D_p^2(1 - \phi_s)^3}{180\phi_s^2\mu_f} \frac{\Delta p_f}{L} \quad (98)$$

462 Our numerical model is validated by modeling fluid flow through a 1m  
 463 long porous media. The porous media is modeled by elastic material with  
 464 Young's modulus is 10 MPa, Poisson's ratio is 0.3, and density is 2650 kg/m<sup>3</sup>.  
 465 The volume fraction of porous media  $\phi_s$  is [0.6, 0.62, 0.66, 0.68, 0.7] and the  
 466 average grain diameter  $d$  is 1mm. The model is discretized in 20 finite element  
 467 and the porous media in 10 finite element with 1 material point per element.  
 468 The pressure gradient is applied with three different value [0.25, 0.5, 1] atm.  
 469 Figure 7 shows a good agreement of fluid flow prediction between the theory  
 470 and the model.

471 *Isothermal consolidation*

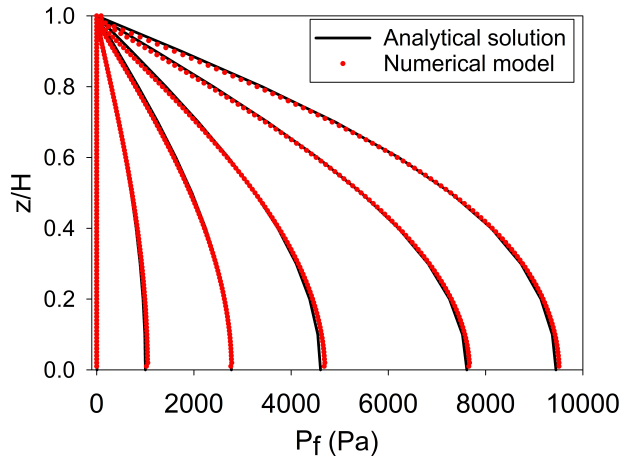


Figure 8: Comparison between analytical solution and numerical solution

472 A common benchmark for a fully saturated porous media is the simulation  
 473 of one-dimensional consolidation. Using the Carman-Kozeny formula, the

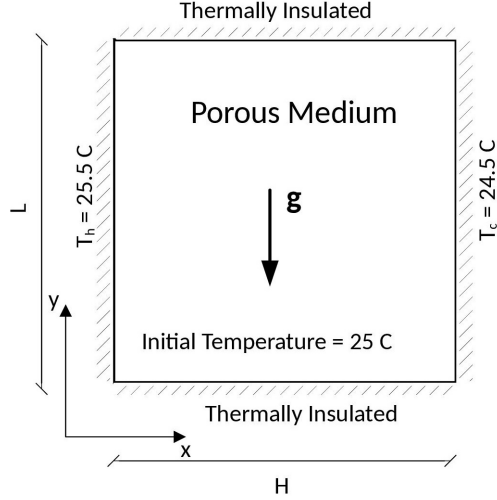


Figure 9: Model schematic [23]

<sup>474</sup> time-dependent pressure can be calculated as:

$$p_f = \sum_{m=1}^{\infty} \frac{2F_{ext}}{M} \sin\left(\frac{Mz}{H}\right) e^{-M^2 T_v} \text{ with } M = \frac{\pi}{2}(2m+1) \quad (99)$$

<sup>475</sup> where the consolidation rate  $T_v = C_v t / H^2$ , the consolidation coefficient  $C_v =$   
<sup>476</sup>  $E_v n^3 d^2 / (180(1-n)^2 \mu)$  and the Oedometer modulus  $E_v = E(1-v)/(1+v)/(1-2v)$ . Our numerical model is validated by modeling the consolidation  
<sup>477</sup> of a 1m column. The porous media is modeled by elastic material with  
<sup>478</sup> Young's modulus is 10 MPa, Poisson's ratio is 0.3, and density is 2650 kg/m<sup>3</sup>.  
<sup>479</sup> The volume fraction of porous media  $\phi_s$  is 0.7 which is equivalent to the  
<sup>480</sup> porosity of 0.3 and the average grain diameter  $d$  is 1mm. The model is  
<sup>481</sup> discretized in 100 finite element with 1 material point per element. The  
<sup>482</sup> external pressure applies to the top of the column is 10 kPa. Figure 8 shows  
<sup>483</sup> a good agreement of fluid flow prediction between the theory and the model.  
<sup>484</sup>

#### <sup>485</sup> Thermal induced cavity flow

<sup>486</sup> Another benchmark is the thermal induced cavity flow in porous me-  
<sup>487</sup> dia. Temperature and velocity distributions are calculated for a square non-  
<sup>488</sup> deformable saturated porous media. The top and bottom walls are insulated,  
<sup>489</sup> and the left and right walls are at fixed temperature gradient of 1 degree. The  
<sup>490</sup> fluid motion at steady state are cavity flow due to the temperature induced

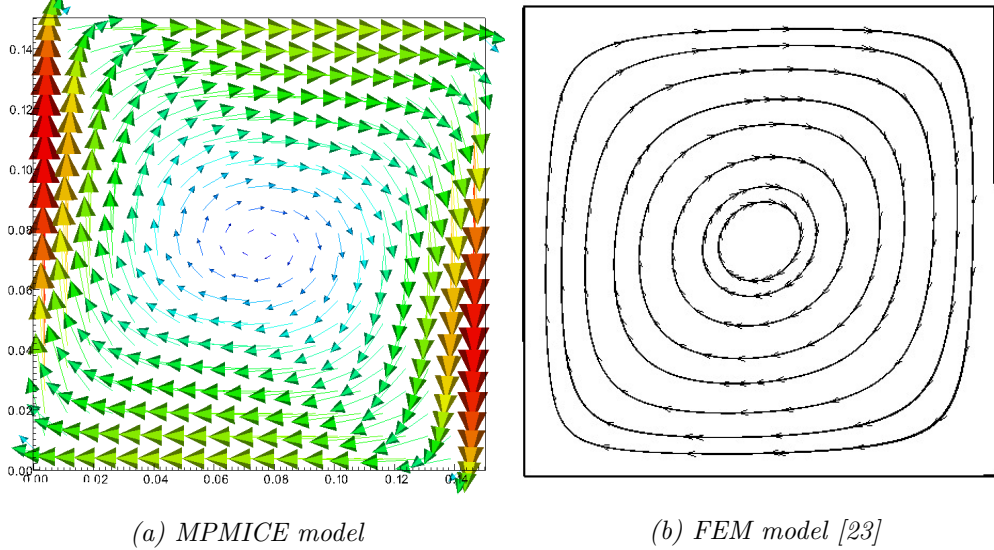
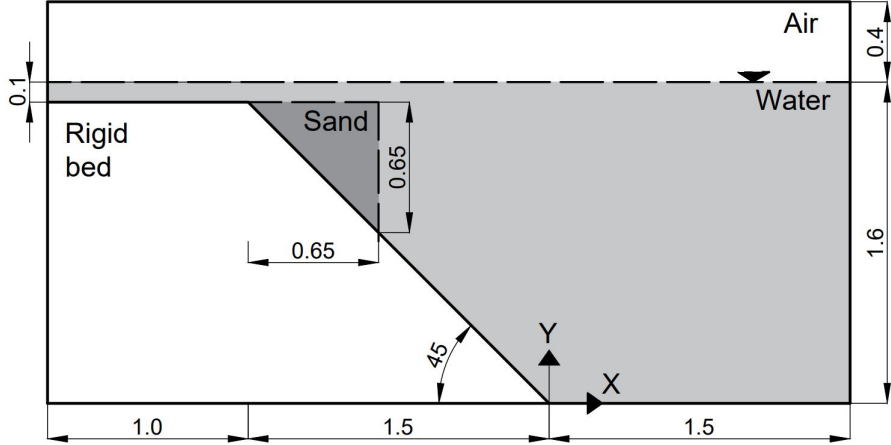


Figure 10: Comparison between MPMICE model and FEM model

491 density variation. The numerical is validated by comparing with the numeri-  
 492 cal solution of the finite element method. The porous media is modeled  
 493 by non deformable material, and density is 2500 kg/m<sup>3</sup>. The specific heat  
 494 capacity of the water and porous skeleton are 4181 J/kg.K and 835 J/kg.K  
 495 respectively. The thermal conductivity of the water and porous skeleton are  
 496 0.598 W/m.K and 0.4 W/m.K. The volume fraction of porous media  $\phi_s$  is 0.6  
 497 which is equivalent to the porosity of 0.4 and the average grain diameter  $d$  is  
 498 1mm. The model is discretized in 20 x 20 finite element with 4 material point  
 499 per element. Figure 10 shows a good agreement of numerical results of the  
 500 model compared with the numerical solution of the finite element method.

#### 501 Underwater debris flow

502 The numerical example is validated using the experimental work of Rzad-  
 503 kiewicz et al. on submarine debris flow [24]. In their experiment, sand within  
 504 a triangular box is released and slides along a rigid bed inclined at 45 degrees  
 505 under water (see Figure 11). The material properties in the numerical model  
 506 are selected based on the experiment by Rzadkiewicz et al. [24]. The sand  
 507 is characterized by a saturated density of 1985 kg/m<sup>3</sup> and a friction angle  
 508 of 10 degrees. The effect of Young's modulus on debris flow run-out is neg-  
 509 ligible due to the extreme deformation of the debris, so a Young's modulus



*Figure 11: Model schematic*

of 50 MPa with a Poisson's ratio of 0.25 is chosen. The rigid bed, being much stiffer, has bulk modulus and shear modulus values of  $117E^7$  Pa and  $43.8E^7$  Pa, respectively. The numerical parameters used in this example are presented in Table 1.

The boundary conditions imposed in the numerical model are as follows: on all boundary faces, the velocity is set to zero ( $U = 0$  m/s) and the temperature is set to 5 degrees Celsius ( $T = 5^\circ\text{C}$ ). At the top boundary, the pressure has a Neumann boundary condition of  $dP/dx = 0$  kPa, and the density has a Neumann boundary condition of  $d\rho/dx = 0 \text{ kg/m}^3$ . The background mesh consists of  $700 \times 400$  cells, resulting in a total of 280,000 cells. Each cell in the debris flow and rigid bed contains  $2 \times 2$  material points.

Figure 13b illustrates snapshots of the underwater debris flow sliding, demonstrating that the model captures the typical hydroplaning mechanism of the debris flow. Hydroplaning refers to the lifting of the debris flow, causing it to lose contact with the bottom layer. The elevation of the free surface at 0.4s and 0.8s is compared between our proposed method and other methods in Figure 12. Our computed results align well with the experimental results [7].

Unlike other computational models that rely on total stress analysis [5, 6, 7, 8], our proposed model utilizes effective stress analysis, enabling the analysis of water pressure and temperature within the debris flow. Additionally, we investigate the differences between underwater debris flow and saturated debris flow in terms of their interaction with obstacles. Figure 13 presents

533 snapshots of simulations of both underwater and saturated debris flow. The  
 534 saturated debris flow (Figure 13a) exhibits behavior similar to frictional flow,  
 535 where grains have contact forces with each other. Conversely, the underwa-  
 536 ter debris flow (Figure 13b) behaves like turbulent flow, with grains being  
 537 separated from each other and exhibiting no contact forces (as reflected by  
 the near-zero effective stress in the turbulence domain).

Materials	Bulk modul (Pa)	Shear modul (Pa)	Density (kg/m <sup>3</sup> )	Temp (C)	Dynamic viscosity (Pa s)	Friction angle (degrees)
Water (at surface)	2.15e9	-	999.8	5	855e-6	-
Air (at top boundary)	-	-	1.177	5	18.45e-6	-
Sand (porous media)	8.33e6	20e6	1985	5	-	10
Rigid bed (solid)	117e7	43.8e7	8900	5	-	-

Table 1: Numerical parameters for the underwater submarine debris

538

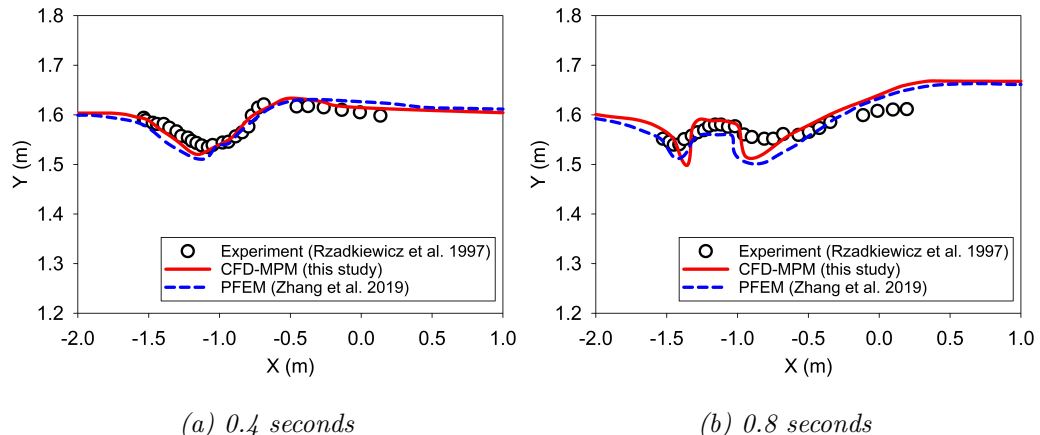


Figure 12: Evolution of water level in the simulation of underwater debris flow

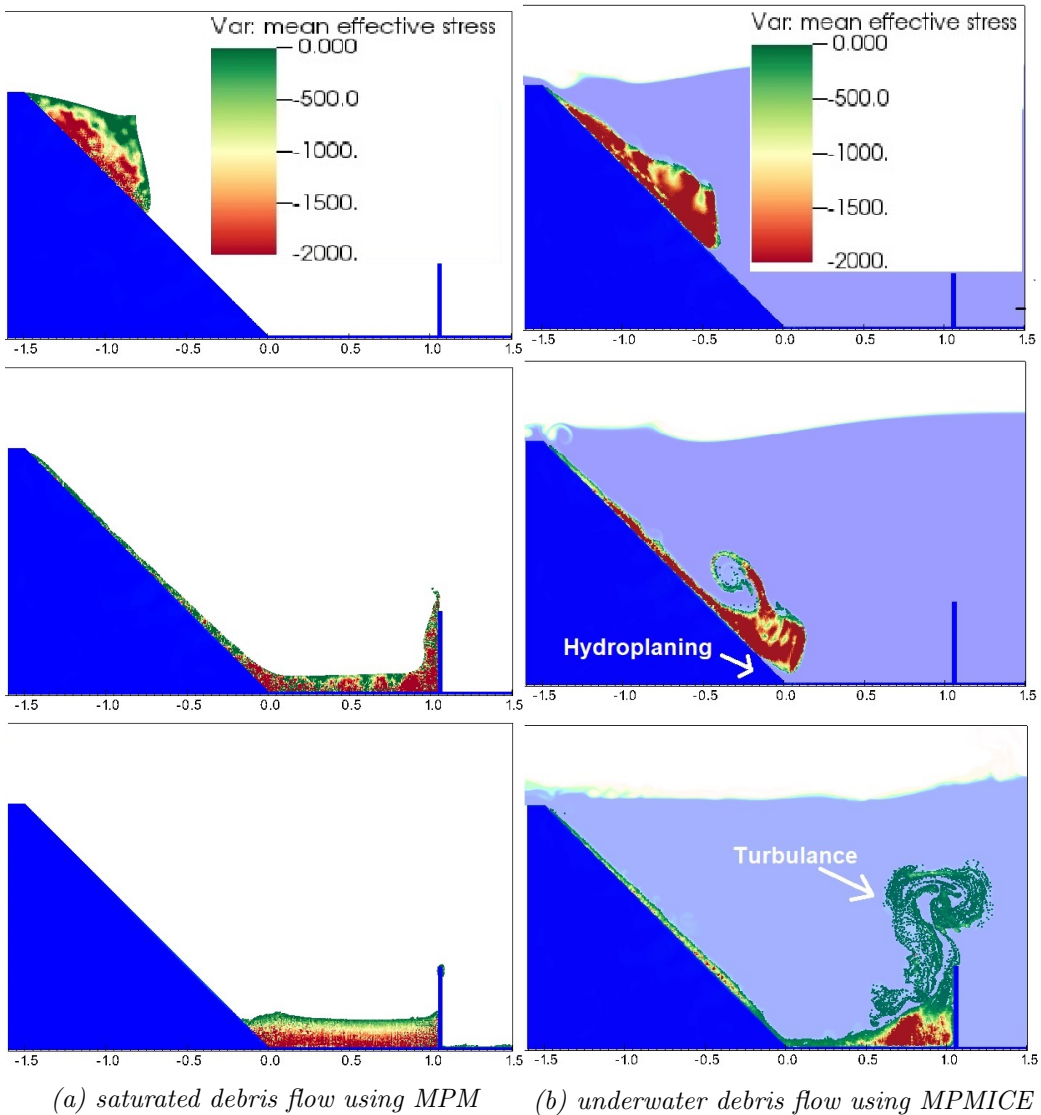


Figure 13: Simulation of Debris Flow: Mean Effective Stress Distribution (Green Color Indicates Near-Zero Effective Stress)

539 *Earthquake-induced submarine landslides*

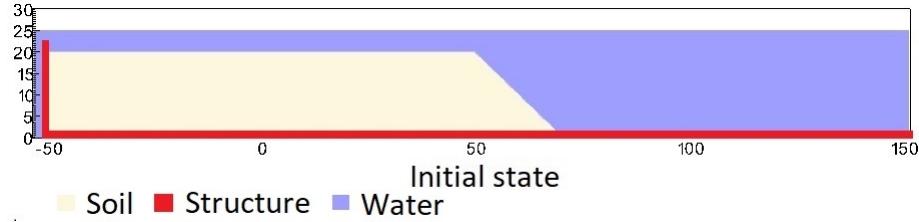


Figure 14: Numerical model of the earthquake-induced submarine landslide

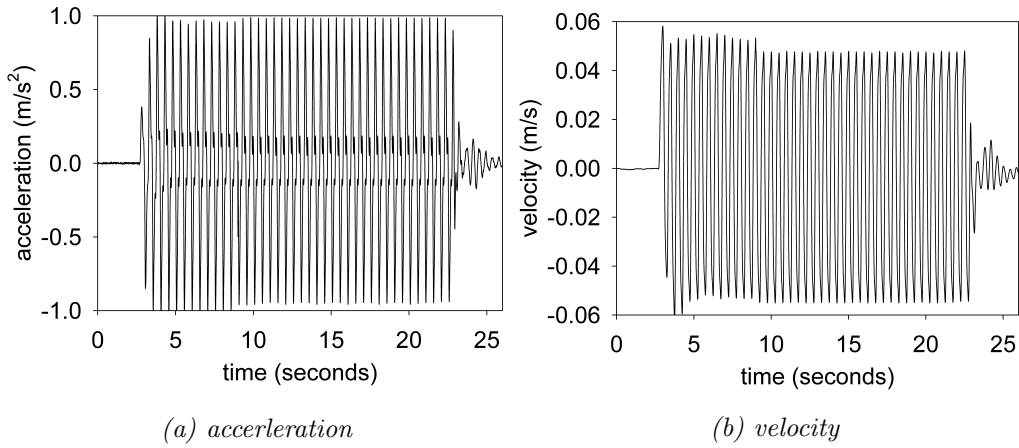


Figure 15: Ground acceleration profile, frequency of 2Hz and magnitude of 1g

540 In the final example, we perform numerical analysis of the earthquake  
 541 induced submarine landslides. A plane strain model with the slope under  
 542 water is shown in Figure 14. A 20m high slope with slope gradient of 45  
 543 degrees is placed in a horizontal and vertical structure which was used to  
 544 be a skaing table to apply earthquake loading. We simplify the earthquake  
 545 loading by simulating the ground shaking for 20 seconds with the constant  
 546 ground acceleration of 1g and a constant frequency of 2Hz (Figure 15a). The  
 547 ground motion is applied in terms of velocity (Figure 15b). An earthquake  
 548 of this magnitude is possible. For instance, in the case of the 2023 Turkey-  
 549 Syria Earthquake, significant ground shaking with peak ground acceleration  
 550 exceeding 1g was observed at numerous locations. This serves as an example

551 of the practical occurrence of such high levels of ground acceleration during  
 552 seismic events.

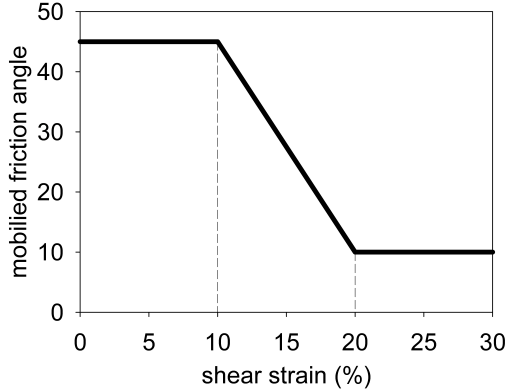
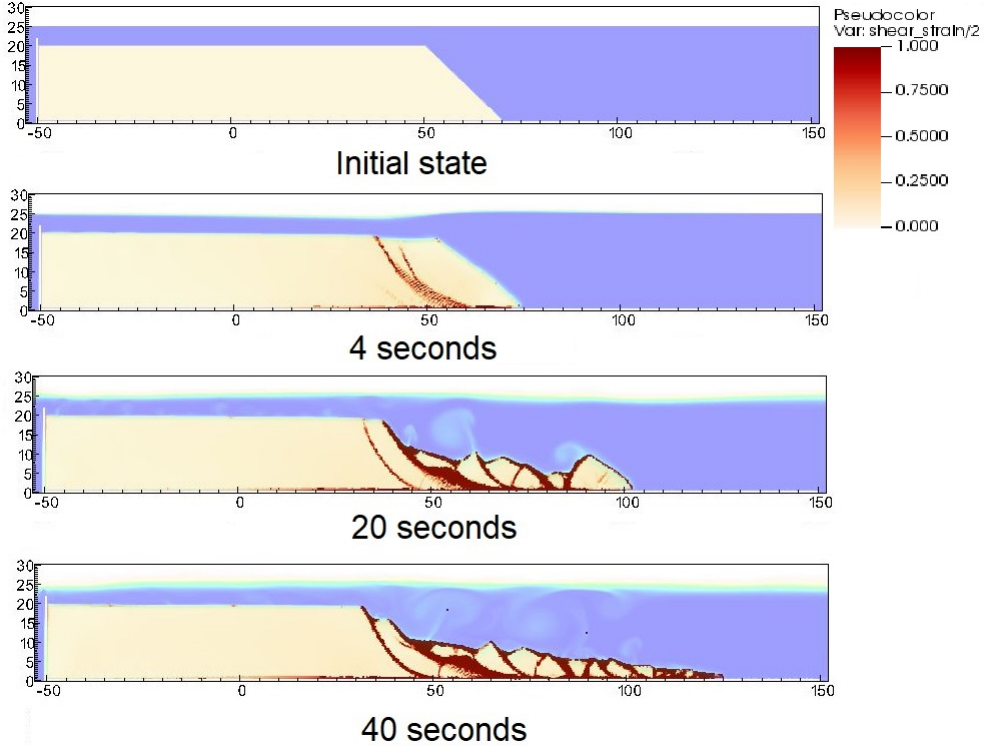


Figure 16: Mobilized friction angle in Mohr Coulomb model

553 A non-associated Mohr-Coulomb model is used for the soil. The soil grain  
 554 has the density of  $2650 \text{ kg/m}^3$ , Young's modulus of 10 kPa and Poisson's  
 555 ratio of 0.3 and zero cohesion. The mobilized friction angle  $\phi'_m$  is governed  
 556 following the softening curve (see Figure 16) with the peak friction angle  $\phi'_p$   
 557 of 45 degrees and the residual friction angle  $\phi'_r$  of 10 degrees. The porosity  
 558 is 0.3 and the average grain size of the soil is around  $0.1 \mu\text{m}$  to mimic the  
 559 undrained behavior. The mobilized dilatancy angle is calculated from the  
 560 Rowe's stress dilatancy theory [25] as follow:

$$\sin \psi'_m = \frac{\sin \phi'_m - \sin \phi'_r}{1 - (\sin \phi'_r \sin \phi'_m)} \quad (100)$$

561 The solid plane is modeled as a rigid body acted as a shaking table. The  
 562 contact between horizontal plane and the sand is the frictional contact with  
 563 the friction coefficient of 0.1. No artificial damping is applied in the simu-  
 564 lation. The contact between vertical plane and the sand is considered to be  
 565 smooth with zero friction coefficient. On all boundary faces, the symmet-  
 566 ric boundary condition is imposed, while the Neumann boundary condition  
 567 is imposed at the top boundary for pressure ( $d\rho/dx = 0 \text{ kPa}$ ) and density  
 568 ( $d\rho/dx = 0 \text{ kg/m}^3$ ). The mesh size is  $0.25 \times 0.25 \text{ m}$  with 300852 element  
 569 cells and 142316 material points. The simulation takes a couple of hours to  
 570 perform 60 seconds of the simulation using 4096 CPUs.



*Figure 17: Shear strain during the earthquake-induced submarine landslides*

571 We demonstrate the entire process and the mechanism of the earthquake-  
 572 induced submarine landslides by showing the shear strain (Figure 17), the  
 573 pore water pressure in atm (Figure 18) and the velocity (Figure 19). The  
 574 failure mechanism can be characterized as the progressive failure mechanism.  
 575 Here are some numerical observation:

- 576 1. At the initial of the seismic event, the seismic loading triggers the  
 577 first slide at 3 seconds. At 4 seconds, the debris start to move with the  
 578 maximum speed of around 2-3 m/s with multiple shear band developed  
 579 in the slope. The wave generated from the submarine slide is around  
 580 2-3m towards the slide direction.

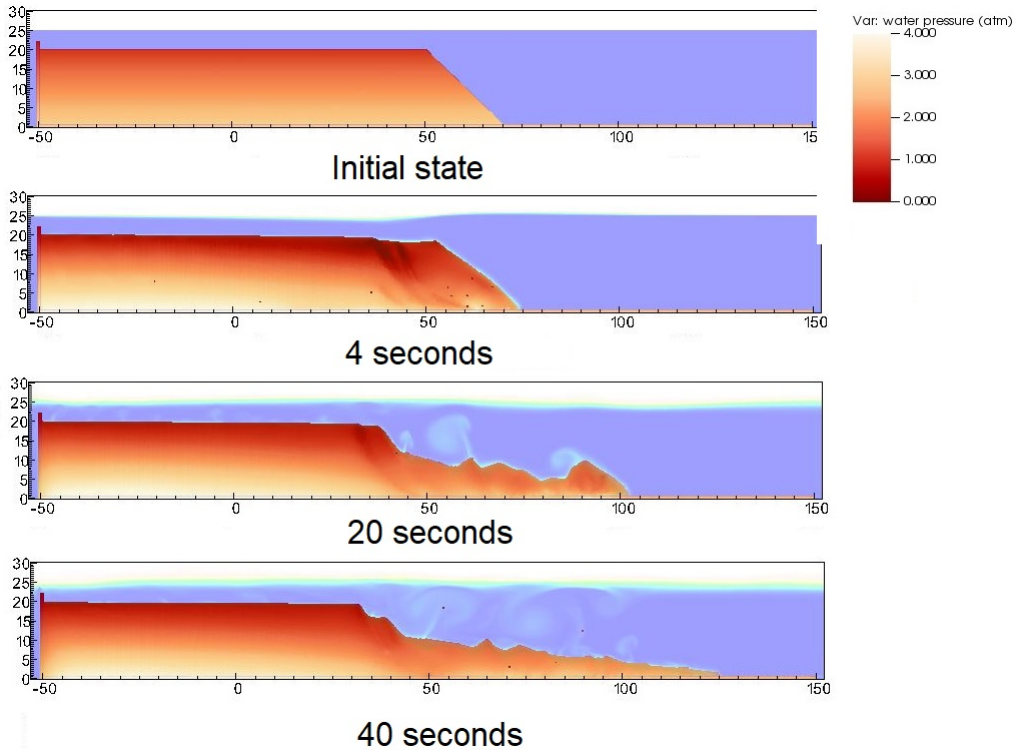


*Figure 18: pore water pressure during the earthquake-induced submarine landslides*

- 581     2. When the onset of the shear band occurs in the slope (for example  
 582       at 4 seconds and 20 seconds), the negative excess pore water pressure  
 583       is developed along this shear band with pore water pressure is under  
 584       1atm. This is a typical dilatancy behavior when the soil is sheared  
 585       rapidly in the undrained behavior.
- 586     3. When the seismic loading ends at 23 seconds, the last shear band is  
 587       mobilized and the slope soon reaches to the final deposition. No more  
 588       progressive failure developed in the slope. The turbulent flow developed  
 589       as the interaction between debris flow and seawater.
- 590     Overall, we show the completed process of the earthquake-induced submarine  
 591       landslides involving (1) earthquake triggering mechanism, (2) the onset of the  
 592       shear band with the development of negative excess pore water pressure, (3)  
 593       progressive failure mechanism, (4) submarine landslide induced wave to final  
 594       deposition.

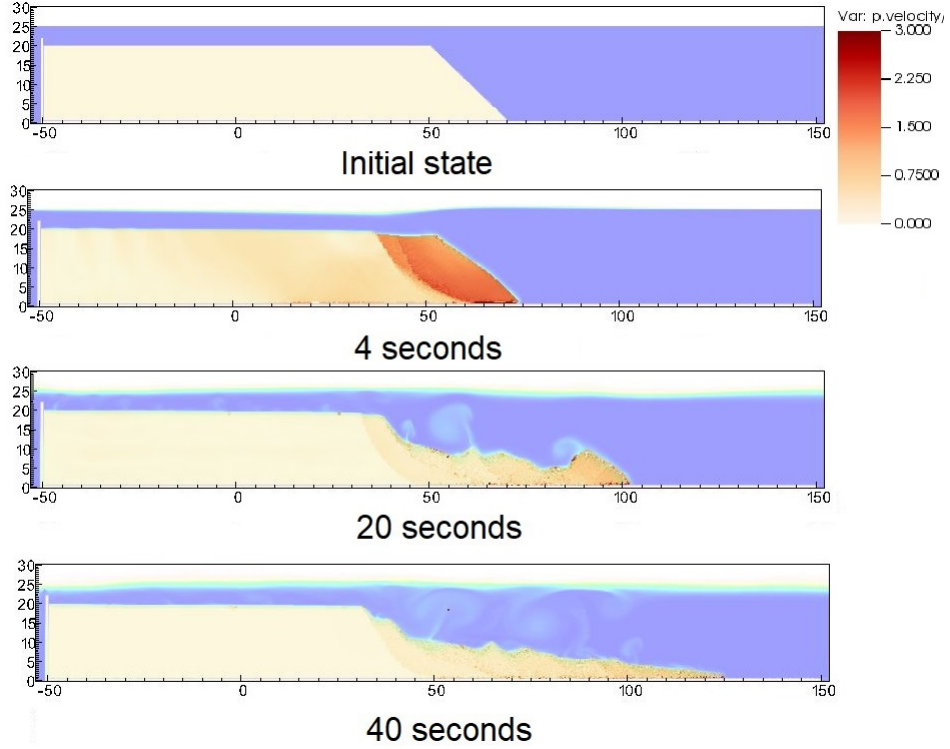


*Figure 19: Velocity during the earthquake-induced submarine landslides*

## 595      **Conclusions**

596      We have presented a numerical approach MPMICE for the simulation  
 597      of large deformation soil-fluid-structure interaction, emphasizing the simu-  
 598      lation of the earthquake-induced submarine landslides. The model uses (1)  
 599      the Material Point Method for capturing the large deformation of iso-thermal  
 600      porous media and solid structures and (2) Implicit Continuous Eulerian (com-  
 601      pressible, conservative multi-material CFD formulation) for modeling the  
 602      complex fluid flow including turbulence. This model is implemented in the  
 603      high-performance Uintah computational framework and validated against an-  
 604      alytical solution and experiment. We then demonstrate the capability of the  
 605      model to simulate the entire process of the earthquake induced submarine  
 606      landslides.

607 **Acknowledgements**

608 The authors gratefully acknowledge Dr. James Guilkey and Dr. Todd  
 609 Harman from the University of Utah for sharing the insight on the theoretical  
 610 framework of MPMICE which this work is based. This project has received  
 611 funding from the European Union's Horizon 2020 research and innovation  
 612 program under the Marie Skłodowska-Curie Actions (MSCA) Individual Fel-  
 613 lowship (Project SUBSLIDE "Submarine landslides and their impacts on  
 614 offshore infrastructures") grant agreement 101022007. The authors would  
 615 also like to acknowledge the support from the Research Council of Norway  
 616 through its Centers of Excellence funding scheme, project number 262644  
 617 Porelab. The computations were performed on High Performance Comput-  
 618 ing resources provided by UNINETT Sigma2 - the National Infrastructure  
 619 for High Performance Computing and Data Storage in Norway.

620 **Appendix: Equation derivation**

621 Before deriving the governing equation, we define the Lagrangian deriva-  
 622 tive for a state variable  $f$  as:

$$\frac{D_f f}{Dt} = \frac{\partial f}{\partial t} + \mathbf{U}_f \cdot \nabla f \quad \frac{D_s f}{Dt} = \frac{\partial f}{\partial t} + \mathbf{U}_s \cdot \nabla f \quad (101)$$

we use some definition following [16] as below:

$$-\frac{1}{V} \left[ \frac{\partial V_f}{\partial p} \right] \equiv \kappa_f \quad \text{isothermal compressibility of fluid} \quad (102)$$

$$\frac{1}{V} \left[ \frac{\partial V_f}{\partial T} \right] \equiv \alpha_f \quad \text{constant pressure thermal expansivity of fluid} \quad (103)$$

623 Then, the rate of volume with incompressible solid grains are calculated as  
 624 belows:

$$\frac{1}{V} \frac{D_f V_f}{Dt} = \frac{1}{V} \left( \left[ \frac{\partial V_f}{\partial p} \right] \frac{D_f P_{eq}}{Dt} + \left[ \frac{\partial V_f}{\partial T_f} \right] \frac{D_f T_f}{Dt} \right) = \frac{1}{V} \left( -\kappa_f \frac{D_f P_{eq}}{Dt} + \alpha_f \frac{D_f T_f}{Dt} \right) \quad (104)$$

625 *Evolution of porosity*

626 Solving the solid mass balance equation (4) with the definition of solid  
 627 mass in equation (2), it leads to the rate of porosity as belows:

$$\frac{D_s m_s}{Dt} = \frac{D_s (\phi_s \rho_s V)}{Dt} = \rho_s V \frac{D_s \phi_s}{Dt} + \phi_s V \frac{D_s \rho_s}{Dt} + \phi_s \rho_s \frac{D_s V}{Dt} = 0 \quad (105)$$

628 The soil grains are assumed to be incompressible, therefore, term 2 in the  
 629 right hand side is zero. leading to:

$$V \frac{D_s \phi_s}{Dt} + \phi_s \frac{D_s V}{Dt} = 0 \quad (106)$$

630 Dividing all terms with  $V$  with the equation  $\frac{1}{V} \frac{D_s V}{Dt} = \nabla \cdot \mathbf{U}_s$ , it leads to:

$$\frac{D_s n}{Dt} = \frac{\partial n}{\partial t} + \mathbf{U}_s \cdot \nabla n = \phi_s \nabla \cdot \mathbf{U}_s \quad (107)$$

631 **Momentum conservation**

632 The linear momentum balance equations for the fluid phases based on  
 633 mixture theory are:

634

$$\frac{1}{V} \frac{D_f(m_f \mathbf{U}_f)}{Dt} = \nabla \cdot (-\phi_f p_f \mathbf{I}) + \nabla \cdot \boldsymbol{\tau}_f + \bar{\rho}_f \mathbf{b} + \sum \mathbf{f}_d + \mathbf{f}_b \quad (108)$$

635 On the right hand sand, the first term is the divergence of partial fluid phase  
 636 stress, the third term is the body force, the fourth term is the drag force  
 637 (momentum exchange) and the fifth term is the buoyant force described in  
 638 [26] for the immiscible mixtures. The buoyant force is in the form as belows:

$$\mathbf{f}_b = \boldsymbol{\sigma}_f \nabla(n) \quad (109)$$

639 As a result, the linear momentum balance equations for the fluid phases  
 640 become as:

$$\frac{1}{V} \frac{D_f(m_f \mathbf{U}_f)}{Dt} = \frac{1}{V} \left[ \frac{\partial(m_f \mathbf{U}_f)}{\partial t} + \nabla \cdot (m_f \mathbf{U}_f \mathbf{U}_f) \right] = -\phi_f \nabla p_f + \nabla \cdot \boldsymbol{\tau}_f + \bar{\rho}_f \mathbf{b} + \sum \mathbf{f}_d \quad (110)$$

641 The Reynolds stress component can be included in the term  $\boldsymbol{\tau}_f$  to consider the  
 642 turbulent effects if needed. To derive the linear momentum balance equation  
 643 for the solid phase, we begin with the linear momentum balance equation for  
 644 the mixture as:

$$\frac{1}{V} \frac{D_f(m_f \mathbf{U}_f)}{Dt} + \frac{1}{V} \frac{D_s(m_s \mathbf{U}_s)}{Dt} = \nabla \cdot (\boldsymbol{\sigma}) + \bar{\rho}_f \mathbf{b} + \bar{\rho}_s \mathbf{b} \quad (111)$$

645 Combining Terzaghi's equation (3) and subtracting both sides with equation  
 646 (110), we obtain the linear momentum balance equations for the solid phase  
 647 as:

$$\frac{1}{V} \frac{D_s(m_s \mathbf{U}_s)}{Dt} = \nabla \cdot (\boldsymbol{\sigma}') - \phi_s \nabla p_f + \bar{\rho}_s \mathbf{b} - \sum \mathbf{f}_d + \sum \mathbf{f}_{fric} \quad (112)$$

648 Here the  $\mathbf{f}_{fric}$  stems from the soil-structure interaction following the contact  
 649 law between the soil/structure interfaces.

650    *Energy conservation*

651    We adopt the general form of the total energy balance equation for the  
 652    porous media from [27], the total energy balance equations for the fluid phases  
 653    are:

$$\frac{1}{V} \frac{D_f(m_f(e_f + 0.5\mathbf{U}_f^2))}{Dt} = \nabla \cdot (-np_f \mathbf{I}) \cdot \mathbf{U}_f + \nabla \cdot \mathbf{q}_f + (\bar{\rho}_f \mathbf{b}) \cdot \mathbf{U}_f + \sum \mathbf{f}_d \cdot \mathbf{U}_f + \sum q_{sf} \quad (113)$$

654    Applying the product rule  $D(m\mathbf{U}^2) = D(m\mathbf{U} \cdot \mathbf{U}) = 2\mathbf{U} \cdot D(m\mathbf{U})$ , the left  
 655    hand side of equation (113) becomes:

656     $\frac{1}{V} \frac{D_f(m_f(e_f + 0.5\mathbf{U}_f^2))}{Dt} = \frac{1}{V} \frac{D_f(m_f e_f)}{Dt} + \frac{1}{V} \frac{D_f(m_f \mathbf{U}_f)}{Dt} \cdot \mathbf{U}_f \quad (114)$

657    Combining equations (110), (113), (114), we obtain the final form of the  
 658    internal energy balance equation for the fluid phases as:

$$\frac{1}{V} \frac{D_f(m_f e_f)}{Dt} = \frac{1}{V} \left[ \frac{\partial(m_f e_f)}{\partial t} + \nabla \cdot (m_f e_f \mathbf{U}_f) \right] = \bar{\rho}_f p_f \frac{D_f v_f}{Dt} + \nabla \cdot \mathbf{q}_f + \sum q_{sf} \quad (115)$$

659    On the right hand side, the terms include the average pressure-volume work,  
 660    the average viscous dissipation, the thermal transport and the energy ex-  
 661    change between solid and fluid respectively. The heat flux is  $\mathbf{q}_f = \bar{\rho}_f \beta_f \nabla T_f$   
 662    with  $\beta_f$  being the thermal conductivity coefficient. To derive the internal  
 663    energy balance equation for the solid phase, we introduce the rate of the  
 664    internal energy for the thermoelastic materials as a function of elastic strain  
 665    tensor  $\boldsymbol{\epsilon}_s^e$  and temperature  $T_s$  as belows:

$$\frac{m_s}{V} \frac{D_s(e_s)}{Dt} = \boldsymbol{\sigma}' : \frac{D_s(\boldsymbol{\epsilon}_s^e)}{Dt} + \frac{D_s(e_s)}{D_s(T_s)} \frac{D_s(T_s)}{Dt} = \boldsymbol{\sigma}' : \frac{D_s(\boldsymbol{\epsilon}_s^e)}{Dt} + c_v \frac{D_s(T_s)}{Dt} \quad (116)$$

666     $c_v$  is the specific heat at the constant volume of the solid materials. The total  
 667    energy balance equation for the mixture based on [27] can be written as:

668    
$$\begin{aligned} \frac{1}{V} \frac{D_f(m_f(e_f + 0.5\mathbf{U}_f^2))}{Dt} + \frac{1}{V} \frac{D_s(m_s(e_s + 0.5\mathbf{U}_s^2))}{Dt} &= \nabla \cdot (-\phi_f p_f \mathbf{I}) \cdot \mathbf{U}_f \\ &+ \nabla \cdot (\boldsymbol{\sigma}' - \phi_s p_f \mathbf{I}) \cdot \mathbf{U}_s + (-\phi_f p_f \mathbf{I}) : \nabla \mathbf{U}_f + \boldsymbol{\sigma}' : \nabla \mathbf{U}_s \\ &+ (\bar{\rho}_f \mathbf{b}) \cdot \mathbf{U}_f + (\bar{\rho}_s \mathbf{b}) \cdot \mathbf{U}_s + \nabla \cdot \mathbf{q}_f + \nabla \cdot \mathbf{q}_s + \sum \mathbf{f}_d \cdot (\mathbf{U}_f - \mathbf{U}_s) \end{aligned} \quad (117)$$

669 Subtracting equation (117), (116) to equations (113) and (112), we obtained  
670 the internal energy balance equation for solid phase as:

$$\boldsymbol{\sigma}' : \frac{D_s(\epsilon_s^e)}{Dt} + \frac{m_s}{V} c_v \frac{D_s(T_s)}{Dt} = \Delta W_s + \Delta W_{friction} + \nabla \cdot \mathbf{q}_s - \sum q_{sf} \quad (118)$$

671 On the right hand side, the terms include the work rate from frictional sliding  
672 between solid materials  $\Delta W_{friction}$ , thermal transport and energy exchange  
673 between solid and fluid respectively. The heat flux is  $\mathbf{q}_s = \bar{\rho}_s \beta_s \nabla T_s$  with  $\beta_s$   
674 being the thermal conductivity of the solid materials, the mechanical work  
675 rate  $\Delta W_s = \boldsymbol{\sigma}' : \frac{D_s(\epsilon_s)}{Dt} = \boldsymbol{\sigma}' : (\frac{D_s(\epsilon_s^e)}{Dt} + \frac{D_s(\epsilon_s^p)}{Dt})$  computed from the constitutive  
676 model with  $\epsilon_s^p$  is the plastic strain tensor, . By subtracting the term  $\boldsymbol{\sigma}' : \frac{D_s(\epsilon_s^e)}{Dt}$ ,  
677 we get the final form of the energy balance equation as:

$$\frac{m_s}{V} c_v \frac{D_s(T_s)}{Dt} = \boldsymbol{\sigma}' : \frac{D_s(\epsilon_s^p)}{Dt} + \Delta W_{friction} + \nabla \cdot \mathbf{q}_s - \sum q_{sf} \quad (119)$$

### 678 Advanced Fluid Pressure

679 The discretization of the pressure equation begins with the Lagrangian  
680 cell face velocity and the equation for the pressure as:

$$\bar{\rho}_{f,FC} \frac{\mathbf{U}_{f,FC}^{n+1} - \mathbf{U}_{f,FC}^n}{dt} = n \nabla^{FC} P_{f,c}^{n+1} + \bar{\rho}_{f,FC} \mathbf{b} \quad (120)$$

$$681 \quad \kappa \frac{dP}{dt} = \nabla^c \cdot \mathbf{U}_{f,FC}^{n+1} \quad (121)$$

682 The divergence of the equation (120) with  $\nabla \cdot \mathbf{b} = 0$  is:

$$\nabla^c \cdot \mathbf{U}_{f,FC}^{n+1} - \nabla^c \cdot \mathbf{U}_{f,FC}^n = \nabla^c \frac{\Delta t}{\rho_{f,FC}^n} \cdot \nabla^{FC} (P_{f,c}^n + \Delta P_{f,c}^n) \quad (122)$$

683 To solve this equation, we define the cell face intermediate velocity  $\mathbf{U}_{f,FC}^*$  as:

$$\bar{\rho}_{f,FC} \frac{\mathbf{U}_{f,FC}^* - \mathbf{U}_{f,FC}^n}{\Delta t} = n \nabla^{FC} P_{f,c}^n + \bar{\rho}_{f,FC} \mathbf{b} \quad (123)$$

684 The divergence of the equation (123) is:

$$\nabla^c \cdot \mathbf{U}_{f,FC}^* - \nabla^c \cdot \mathbf{U}_{f,FC}^n = \nabla^c \frac{\Delta t}{\rho_{f,FC}^n} \cdot \nabla^{FC} P_{f,c}^n \quad (124)$$

685 Combining equations (121, 122, 124), it leads to:

$$\left( \kappa - \nabla^c \frac{\Delta t}{\rho_{f,FC}^n} \cdot \nabla^{FC} \right) \Delta P_{fc}^n = -\nabla^c \cdot \mathbf{U}_{f,FC}^* \quad (125)$$

686 When the fluid is incompressible,  $\kappa$  approaches to zero and the equation  
687 (125) becomes the Poisson's equation for the incompressible fluid flow.

688 *Momentum and Energy exchange with an implicit solver*

689 Considering the fluid momentum balance equation as:

$$(m\mathbf{U})_{f,FC}^{n+1} = (m\mathbf{U})_{f,FC}^n - \Delta t(Vn\nabla^{FC}P_{f,c}^n + m_f\mathbf{b}) + VK\Delta t(\mathbf{U}_{s,FC}^{n+1} - \mathbf{U}_{f,FC}^{n+1}) \quad (126)$$

690 And assuming  $m_{f,FC}^{n+1} = m_{f,FC}^n$ , we get:

$$\mathbf{U}_{f,FC}^{n+1} = \mathbf{U}_{f,FC}^n - \Delta t\left(\frac{\nabla^{FC}P_{fc}^n}{\rho_{f,FC}^n} + \mathbf{b}\right) + \frac{\Delta tK}{\bar{\rho}_{f,FC}^n}(\mathbf{U}_{s,FC}^{n+1} - \mathbf{U}_{f,FC}^{n+1}) \quad (127)$$

691 As defined in the section 'Advanced Fluid Pressure', the cell face intermediate  
692 fluid velocity  $\mathbf{U}_{f,FC}^* = \Delta t(\nabla^{FC}P_{fc}^n/\rho_{f,FC}^n + \mathbf{b})$  is computed as:

$$\mathbf{U}_{f,FC}^{n+1} = \mathbf{U}_{f,FC}^* + \frac{\Delta tK}{\bar{\rho}_{f,FC}^n}(\mathbf{U}_{s,FC}^{n+1} - \mathbf{U}_{f,FC}^{n+1}) \quad (128)$$

693 Considering the solid momentum balance equation as:

$$(m\mathbf{U})_{s,FC}^{n+1} = (m\mathbf{U})_{s,FC}^n - \Delta t(V\nabla^{FC} \cdot \boldsymbol{\sigma}'^n - V(1-n)\nabla^{FC}P_{f,c}^n + m_s\mathbf{b}) - VK\Delta t(\mathbf{U}_{s,FC}^{n+1} - \mathbf{U}_{f,FC}^{n+1}) \quad (129)$$

694 We define the cell face intermediate solid velocity as  $\mathbf{U}_{s,FC}^* = \Delta t(\nabla^{FC} \cdot \boldsymbol{\sigma}'^n / \bar{\rho}_{s,FC}^n - \nabla^{FC}P_{f,c}^n/\rho_s + \mathbf{b})$  leading to:

$$\mathbf{U}_{s,FC}^{n+1} = \mathbf{U}_{s,FC}^* - \frac{\Delta tK}{\bar{\rho}_{s,FC}^n}(\mathbf{U}_{s,FC}^{n+1} - \mathbf{U}_{f,FC}^{n+1}) \quad (130)$$

696 Combining equation (128) and (130) we get:

$$\begin{aligned} \mathbf{U}_{f,FC}^* + \Delta\mathbf{U}_{f,FC} &= \mathbf{U}_{f,FC}^* + \frac{\Delta tK}{\bar{\rho}_{f,FC}^n}(\mathbf{U}_{s,FC}^* + \Delta\mathbf{U}_{s,FC} - \mathbf{U}_{f,FC}^* - \Delta\mathbf{U}_{f,FC}) \\ \mathbf{U}_{s,FC}^* + \Delta\mathbf{U}_{s,FC} &= \mathbf{U}_{s,FC}^* - \frac{\Delta tK}{\bar{\rho}_{s,FC}^n}(\mathbf{U}_{s,FC}^* + \Delta\mathbf{U}_{s,FC} - \mathbf{U}_{f,FC}^* - \Delta\mathbf{U}_{f,FC}) \end{aligned} \quad (131)$$

697 Rearranging the equation (131), it leads to the linear system of equations as  
 698 belows:

$$\begin{vmatrix} (1 + \beta_{12,FC}) & -\beta_{12,FC} \\ -\beta_{21,FC} & (1 + \beta_{21,FC}) \end{vmatrix} \begin{vmatrix} \Delta \mathbf{U}_{f,FC} \\ \Delta \mathbf{U}_{s,FC} \end{vmatrix} = \begin{vmatrix} \beta_{12,FC}(\mathbf{U}_{s,FC}^* - \mathbf{U}_{f,FC}^*) \\ \beta_{21,FC}(\mathbf{U}_{f,FC}^* - \mathbf{U}_{s,FC}^*) \end{vmatrix}$$

699 Solving this linear equations with  $\beta_{12,FC} = (\Delta t K) / \bar{\rho}_{f,FC}^n$  and  $\beta_{21,FC} =$   
 700  $(\Delta t K) / \bar{\rho}_{s,FC}^n$  with K is the momentum exchange coefficient. Similar deriva-  
 701 tion can be performed to computed the cell-center velocity increment leading  
 702 to:

$$\begin{vmatrix} (1 + \beta_{12c}) & -\beta_{12c} \\ -\beta_{21c} & (1 + \beta_{21c}) \end{vmatrix} \begin{vmatrix} \Delta \mathbf{U}_{f,c} \\ \Delta \mathbf{U}_{sc} \end{vmatrix} = \begin{vmatrix} \beta_{12c}(\mathbf{U}_{sc}^* - \mathbf{U}_{f,c}^*) \\ \beta_{21c}(\mathbf{U}_{f,c}^* - \mathbf{U}_{sc}^*) \end{vmatrix}$$

703 with  $\beta_{12c} = (\Delta t K) / \bar{\rho}_{f,c}^n$  and  $\beta_{21c} = (\Delta t K) / \bar{\rho}_{sc}^n$  and the cell-centered interme-  
 704 diate velocity can be calculated by:

$$\begin{aligned} \mathbf{U}_{f,c}^* &= \mathbf{U}_{f,c}^n + \Delta t \left( -\frac{\nabla P_{f,c}^{n+1}}{\rho_{f,c}^n} + \frac{\nabla \cdot \boldsymbol{\tau}_{f,c}^n}{\bar{\rho}_{f,c}^n} + \mathbf{b} \right) \\ \mathbf{U}_{sc}^* &= \mathbf{U}_{sc}^n + \Delta t \left( \frac{\nabla \cdot \boldsymbol{\sigma}_c'^n}{\bar{\rho}_{sc}^n} - \frac{\nabla P_{f,c}^{n+1}}{\rho_s} + \mathbf{b} \right) \end{aligned} \quad (132)$$

705 For generalize multi materials i,j = 1:N, the linear equations is in the form  
 706 as:

$$\begin{vmatrix} (1 + \beta_{ij}) & -\beta_{ij} \\ -\beta_{ji} & (1 + \beta_{ji}) \end{vmatrix} \begin{vmatrix} \Delta \mathbf{U}_i \\ \Delta \mathbf{U}_j \end{vmatrix} = \begin{vmatrix} \beta_{ij}(\mathbf{U}_i^* - \mathbf{U}_j^*) \\ \beta_{ji}(\mathbf{U}_j^* - \mathbf{U}_i^*) \end{vmatrix}$$

707 Similar approach applied for the ernergy exchange term leading to:

$$\begin{vmatrix} (1 + \eta_{ij}) & -\eta_{ij} \\ -\eta_{ji} & (1 + \eta_{ji}) \end{vmatrix} \begin{vmatrix} \Delta T_i \\ \Delta T_j \end{vmatrix} = \begin{vmatrix} \eta_{ij}(T_i^n - T_j^n) \\ \eta_{ji}(T_j^n - T_i^n) \end{vmatrix}$$

708 with  $\eta$  is the energy exchange coefficient.

## 709 References

- 710 [1] D. Yuk, S. Yim, P.-F. Liu, Numerical modeling of submarine mass-  
 711 movement generated waves using RANS model, Computers and Geo-  
 712 sciences 32 (7) (2006) 927–935. doi:10.1016/j.cageo.2005.10.028.  
 713 URL <https://doi.org/10.1016/j.cageo.2005.10.028>

- 714 [2] S. Glimsdal, J.-S. L'Heureux, C. B. Harbitz, F. Løvholt, The 29th january 2014 submarine landslide at statland, norway—landslide dynamics,  
715 tsunami generation, and run-up, *Landslides* 13 (6) (2016) 1435–1444.  
716 doi:10.1007/s10346-016-0758-7.  
717 URL <https://doi.org/10.1007/s10346-016-0758-7>
- 718 [3] S. Abadie, D. Morichon, S. Grilli, S. Glockner, Numerical simulation of waves generated by landslides using a multiple-fluid navier–stokes model, *Coastal Engineering* 57 (9) (2010) 779–794.  
719 doi:10.1016/j.coastaleng.2010.03.003.  
720 URL <https://doi.org/10.1016/j.coastaleng.2010.03.003>
- 721 [4] M. Rauter, S. Viroulet, S. S. Gylfadóttir, W. Fellin, F. Løvholt, Granular  
722 porous landslide tsunami modelling – the 2014 lake askja flank collapse,  
723 *Nature Communications* 13 (1) (Feb. 2022). doi:10.1038/s41467-022-  
724 28296-7.  
725 URL <https://doi.org/10.1038/s41467-022-28296-7>
- 726 [5] Q.-A. Tran, W. Sołowski, Generalized interpolation material point  
727 method modelling of large deformation problems including strain-rate  
728 effects – application to penetration and progressive failure problems,  
729 *Computers and Geotechnics* 106 (2019) 249–265.  
730 doi:10.1016/j.compgeo.2018.10.020.  
731 URL <https://doi.org/10.1016/j.compgeo.2018.10.020>
- 732 [6] T. Capone, A. Panizzo, J. J. Monaghan, SPH modelling of water  
733 waves generated by submarine landslides, *Journal of Hydraulic Research*  
734 48 (sup1) (2010) 80–84. doi:10.1080/00221686.2010.9641248.  
735 URL <https://doi.org/10.1080/00221686.2010.9641248>
- 736 [7] X. Zhang, E. Oñate, S. A. G. Torres, J. Bleyer, K. Krabbenhoft, A  
737 unified lagrangian formulation for solid and fluid dynamics and its possi-  
738 bility for modelling submarine landslides and their consequences, *Computer  
739 Methods in Applied Mechanics and Engineering* 343 (2019) 314–  
740 338. doi:10.1016/j.cma.2018.07.043.  
741 URL <https://doi.org/10.1016/j.cma.2018.07.043>
- 742 [8] R. Dey, B. C. Hawlader, R. Phillips, K. Soga, Numerical modelling  
743 of submarine landslides with sensitive clay layers, *Géotechnique* 66 (6)
- 744

- 747 (2016) 454–468. doi:10.1680/jgeot.15.p.111.  
748 URL <https://doi.org/10.1680/jgeot.15.p.111>
- 749 [9] S. Bandara, K. Soga, Coupling of soil deformation and pore fluid flow  
750 using material point method, Computers and Geotechnics 63 (2015)  
751 199–214. doi:10.1016/j.compgeo.2014.09.009.  
752 URL <https://doi.org/10.1016/j.compgeo.2014.09.009>
- 753 [10] A. P. Tampubolon, T. Gast, G. Klár, C. Fu, J. Teran, C. Jiang,  
754 K. Museth, Multi-species simulation of porous sand and water  
755 mixtures, ACM Transactions on Graphics 36 (4) (2017) 1–11.  
756 doi:10.1145/3072959.3073651.  
757 URL <https://doi.org/10.1145/3072959.3073651>
- 758 [11] A. S. Baumgarten, K. Kamrin, A general constitutive model for dense,  
759 fine-particle suspensions validated in many geometries, Proceedings  
760 of the National Academy of Sciences 116 (42) (2019) 20828–20836.  
761 doi:10.1073/pnas.1908065116.  
762 URL <https://doi.org/10.1073/pnas.1908065116>
- 763 [12] Q.-A. Tran, W. Sołowski, Temporal and null-space filter for the  
764 material point method, International Journal for Numerical Methods in  
765 Engineering 120 (3) (2019) 328–360. doi:10.1002/nme.6138.  
766 URL <https://doi.org/10.1002/nme.6138>
- 767 [13] X. Zheng, F. Pisanò, P. J. Vardon, M. A. Hicks, An explicit stabilised  
768 material point method for coupled hydromechanical problems in two-  
769 phase porous media, Computers and Geotechnics 135 (2021) 104112.  
770 doi:10.1016/j.compgeo.2021.104112.  
771 URL <https://doi.org/10.1016/j.compgeo.2021.104112>
- 772 [14] Q. A. Tran, W. Sołowski, M. Berzins, J. Guilkey, A convected particle  
773 least square interpolation material point method, International Journal  
774 for Numerical Methods in Engineering 121 (6) (2019) 1068–1100.  
775 doi:10.1002/nme.6257.  
776 URL <https://doi.org/10.1002/nme.6257>
- 777 [15] J.-S. Chen, M. Hillman, S.-W. Chi, Meshfree methods: Progress made  
778 after 20 years, Journal of Engineering Mechanics 143 (4) (Apr. 2017).

- 779 doi:10.1061/(asce)em.1943-7889.0001176.  
780 URL [https://doi.org/10.1061/\(asce\)em.1943-7889.0001176](https://doi.org/10.1061/(asce)em.1943-7889.0001176)
- 781 [16] B. A. Kashiwa, A multifield model and method for fluid-structure in-  
782 teraction dynamics, Tech. Rep. LA-UR-01-1136, Los Alamos National  
783 Laboratory (2001).
- 784 [17] J. Guilkey, T. Harman, B. Banerjee, An eulerian-lagrangian  
785 approach for simulating explosions of energetic devices,  
786 Computers and Structures 85 (11) (2007) 660 – 674.  
787 doi:<https://doi.org/10.1016/j.compstruc.2007.01.031>.  
788 URL <http://www.sciencedirect.com/science/article/pii/S0045794907000429>
- 789 [18] A. S. Baumgarten, B. L. Couchman, K. Kamrin, A coupled finite volume  
790 and material point method for two-phase simulation of liquid-sediment  
791 and gas-sediment flows, Computer Methods in Applied Mechanics and  
792 Engineering 384 (2021) 113940. doi:10.1016/j.cma.2021.113940.  
793 URL <https://doi.org/10.1016/j.cma.2021.113940>
- 794 [19] S. Bardenhagen, J. Guilkey, K. Roessig, J. Brackbill, W. Witzel,  
795 J.C.Foster, An improved contact algorithm for the material point  
796 method and application to stress propagation in granular material,  
797 CMES-Computer Modeling in Engineering and Sciences 2 (2001) 509–  
798 522. doi:10.3970/cmes.2001.002.509.
- 799 [20] J. A. M. K. R. Beetstra, M. A. van der Hoef, Drag force of interme-  
800 diate reynolds number flow past mono- and bidisperse arrays of spheres,  
801 Fluid Mechanics and Transport Phenomena 53 (2) (2007) 489 – 501.  
802 doi:<https://doi.org/10.1002/aic.11065>.
- 803 [21] R. W. Stewart, The air-sea momentum exchange, Boundary-Layer Me-  
804 teorology 6 (1-2) (1974) 151–167. doi:10.1007/bf00232481.  
805 URL <https://doi.org/10.1007/bf00232481>
- 806 [22] S. G. B. amd E. M. Kober, The generalized interpolation material point  
807 method, Computer Modeling in Engineering and Sciences 5 (2004) 477–  
808 496. doi:10.1016/j.compgeo.2021.104199.  
809 URL <https://doi.org/10.3970/cmes.2004.005.477>
- 810 [23] S. G. Amiri, E. Taheri, A. Lavasan, A hybrid finite element model for  
811 non-isothermal two-phase flow in deformable porous media, Computers

- 812 and Geotechnics 135 (2021) 104199. doi:10.1016/j.compgeo.2021.104199.  
813 URL <https://doi.org/10.1016/j.compgeo.2021.104199>
- 814 [24] S. A. R. C. Mariotti;, P. Heinrich, Numerical simulation of sub-  
815 marine landslides and their hydraulic effects, Journal of Waterway, Port,  
816 Coastal, and Ocean Engineering 123 (4) (1997).  
817 doi:[https://doi.org/10.1061/\(ASCE\)0733-950X\(1997\)123:4\(149\)](https://doi.org/10.1061/(ASCE)0733-950X(1997)123:4(149)).
- 818 [25] D. Muir Wood, Soil behaviour and critical state soil mechanics, Cam-  
819 bridge University Press, United Kingdom, 1990.
- 820 [26] D. Drumheller, On theories for reacting immiscible mixtures, Interna-  
821 tional Journal of Engineering Science 38 (3) (2000) 347 – 382.  
822 doi:[https://doi.org/10.1016/S0020-7225\(99\)00047-6](https://doi.org/10.1016/S0020-7225(99)00047-6).  
823 URL <http://www.sciencedirect.com/science/article/pii/S0020722599000476>
- 824 [27] S. Hassanzadeh, Derivation of basic equations of mass transport in  
825 porous media, part1: Macroscopic balance laws, Advances in Wa-  
826 ter Resources 9 (1986) 196–206. doi:[https://doi.org/10.1016/0309-1708\(86\)90024-2](https://doi.org/10.1016/0309-1708(86)90024-2).